Satellite Sampling and Retrieval Errors in Regional Monthly Rain Estimates from TMI AMSR-E, SSM/I, AMSU-B and the TRMM PR

Brad Fisher[1,2] and David B. Wolff[1,2]

[1] *Science Systems and Applications, Inc., Lanham, MD*

[2]*NASA Goddard Space Flight Center, Greenbelt, Maryland*

Submitted to

Journal of Applied Meteorology and Climatology

Re-Submitted on July 26, 2010

ABSTRACT

Passive and active microwave rain sensors onboard earth-orbiting satellites estimate monthly rainfall from the instantaneous rain statistics collected during satellite overpasses. It is well known that climate-scale rain estimates from meteorological satellites incur sampling errors resulting from the process of discrete temporal sampling and statistical averaging. Sampling and retrieval errors ultimately become entangled in the estimation of the mean monthly rain rate. The sampling component of the error budget effectively introduces statistical noise into climate-scale rain estimates that obscure the error component associated with the instantaneous rain retrieval. Estimating the accuracy of the retrievals on monthly scales therefore necessitates a decomposition of the total error budget into sampling and retrieval error quantities.

This paper presents results from a statistical evaluation of the sampling and retrieval errors for five different space-borne rain sensors on board nine orbiting satellites. Using an error decomposition methodology developed by one of the authors, sampling and retrieval errors were estimated at 0.25° resolution within 150 km of ground-based weather radars located at Kwajalein, Marshall Islands and Melbourne, Florida. Error and bias statistics were calculated according to the land, ocean and coast classifications of the surface terrain mask developed for the Goddard Profiling (GPROF) rain algorithm. Variations in the comparative error statistics are attributed to various factors related to differences in the swath geometry of each rain sensor, the orbital and instrument characteristics of the satellite and the regional climatology. The most significant result from this study found that each of the satellites incurred negative long-term oceanic retrieval biases of 10 to 30%.

1. Introduction

Meteorological satellites offer a practical, cost effective strategy of globally monitoring the circulation of water and energy in the atmosphere. Over the past twenty-five years, technological advancements in microwave technology and algorithmic improvements in the rain retrievals have significantly reduced uncertainties in satellite-observed rain rate retrievals. Recent studies have shown that the TRMM microwave imager (TMI) and the Advanced Microwave Scanning Radiometer (AMSR-E) can now replicate the rain rate distributions inferred from gauge-calibrated ground radars with impressive accuracy (Liu and Hou 2008, Wolff and Fisher 2009). However, significant uncertainties still exist due to the presence of sampling and retrieval errors in the monthly rainfall estimates (Wilheit, 1988, Laughlin 1981, McConnell and North 1987, Shin and North 1988, North 1988, Oki 1994, Steiner 1996, Bell and Kundu 2000, Fisher 2004, 2007).

It is in the monthly rain statistics that sampling and retrieval errors become entangled. An orbiting satellite, for example, only spends a few moments per day retrieving rainfall information over a fixed grid box on the earth's surface, which over a month produces a temporally discrete time series of instantaneous snapshots separated by large time intervals. On average the satellite collects samples at a rate of between one to three samples per day over any 0.25° x 0.25° region in the sampling domain of the satellite. Monthly rain amounts must therefore be estimated from the unconditional mean rain rate as determined from a time series where most of the data is effectively missing.

Sampling errors represent the mean uncertainty in the estimate due to the existence of large time gaps in the time series, defined as the difference between the

observed mean rain rate and the rain rate that would be estimated if the satellite measured the rainfall continuously. Retrieval errors, in contrast, can be defined as the difference between the retrieved and the actual rain rates when the satellite is overhead. Retrieval errors are largely attributed to the uncertainty in the radiometric measurement and the inversion process that produces retrieval of rain rates from the calibrated radiance measurement. Retrieval errors can also vary depending on a particular scene or rain climatology.

In this study we will statistically quantify and assess the sampling and retrieval errors estimated at 0.25°- grid spacing for eight different satellites equipped with precipitation sensor. Table 1 furnishes a listing of the satellites in this study, along with the orbital and instrument characteristics of the rain sensors on board. The study analyzed data from four types of passive microwave rain sensors, including the TRMM Microwave Imager (TMI), the United States Defense Department's Special Sensor Microwave Imager (SSM/I), the National Oceanic Atmospheric Administration's Advanced Microwave Scanning Radiometer (AMSR-E), and the Advanced Microwave Sounding Unite (AMSU), as well as a space-borne precipitation radar (PR) that complements the TMI on board the TRMM satellite. In this analysis we also analyzed the retrieval errors the TRMM Combined (COM 2B31) rain product, which integrates rain information from the TRMM microwave imager (TMI 2A12) and the PR to produce hybrid rain retrievals.

The sampling design of the Tropical Rainfall Measuring Mission (TRMM) satellite is especially noteworthy, for unlike the other satellites in Table 1, it flies in a sun-asynchronous orbit and is thus able to sample thediurnal cycle over about a 46-day mean period. The sampling frequency and the aperiodic variance in the sampling

frequency are both a function of latitude. TRMM collects more samples at higher latitudes near the satellite turning point. However, the sampling frequency is more highly variable because of the close conjunction of ascending and descending orbits near the satellite turning point. The satellite precession subsequently produces secondary sampling periods, some which are very short and some, which are very long (Negri et al., 2002). The other passive microwave (PMW) rain sensors fly in sun-synchronous, polar orbits and collect two samples per day at a near-constant sampling frequency for a given grid box. TRMM's sampling design was intended to provide more representative rain statistics of the diurnal cycle.

We estimated long-term sampling and retrieval errors and biases using the statistical decomposition methodology developed by Fisher (2004, 2007). This error model was applied to six years (2003-2008) of satellite data over two TRMM Ground Validation (GV) sites: Kwajalein (KWAJ) in the Central Pacific and Melbourne, Florida (MELB). The method decomposes the errors using monthly and instantaneous radar-inferred rain estimates averaged at the satellite resolution of 0.25° and sub-sampled during satellite overpasses of the GV site. KWAJ and MELB provide two contrasting climate regimes for evaluating error characteristics associated with each sensor. KWAJ is strategically located in the Inter-Tropical Convergence Zone and represents a pure open ocean site. The rainfall climatology of MELB is strongly influence by land-sea interaction and from the standpoint of satellite sampling is located at a higher latitude.

This study is presented in seven sections. Section 2 provides a review of the published literature and further background on the nature of the sampling and retrieval of rainfall by satellites. Section 3 gives a description of the data used in the study. Section 4

explains the methodology. Section 5 considers diurnal and seasonal patterns of surface rainfall as observed by each of the satellites and its effects on sampling and retrievals. Section 6 statistically evaluates the sampling and retrieval errors from each sensor class at 0.25 and 0.50 scales. Section 7 will provide a summary and discussion of the results.

2. Background

To understand how sampling and retrieval errors become entangled in the monthly estimate, consider a single instantaneous overpass of an arbitrary grid box of area **A** in the sampling domain of the satellite and assume that the swath of the rain sensor samples the entire grid box (i.e., complete coverage). We can now define the instantaneous retrieval error $\boldsymbol{\varepsilon_{ret}}$ at time t during a single satellite overpass of **A** as the difference between the observed rain rate $\mathbf{s_0(x_A, t)}$ and the true rain mean areal rate $\mathbf{r_T(x_A,t)}$:

$$\varepsilon_{ret} = s_0(x_A, t) - r_T(x_A, t) \tag{1}$$

where x_A denotes the area defined by A. The instantaneous retrieval error defined in (1) represents the mean retrieval error averaged over the entire area of the grid box and characterizes the error associated with a single measurement of instantaneous surface rainfall.

Now consider the satellite's estimation of monthly rainfall. An orbiting satellite cannot continuously sample the grid box (as defined by **A)** continuously, and instead typically collects about 1 to 3 instantaneous snapshots per day. For an arbitrarily selected grid box, the mean monthly rainfall is estimated from the total number of observations in one month. The total error ξ_{err} for any given month is then defined as the difference

between the observed monthly rainfall for the satellite $\mathbf{S_0}$ and the true mean monthly rainfall $\mathbf{R_T}$,

$$\xi_{tot} = S_0 - R_T, \tag{2}$$

where $\mathbf{S_0}$ and $\mathbf{R_T}$ are defined as:

$$S_0 = \frac{1}{N}\sum_{i=1}^{N} \omega_i s_0(x_A, t_i) \tag{3a}$$

$$R_T = \frac{1}{T}\int_0^T dt \int_A r_T(x_A, t) dA \tag{3b}$$

The parameter $\boldsymbol{\omega_i}$ in (3a) represents a weighting factor that accounts for the partial coverage of the gridbox and **N** represents the total number of satellite overpasses of **A** for a single month. In (3b), **T** denotes the time granule, which in this study is equal to a single month (Bell et al. 2001, Fisher 2007).

In addition to the retrieval error, some of the difference between the true and observed monthly rainfall results from the non-continuous sampling of the gridbox. If there was no retrieval error, the sampling error would be defined as the difference between the expressions in (3a) and (3b). The sampling and retrieval of monthly rainfall are illustrated in Figs. 1a and 1b. The rectangular region shown on the left side of Fig 1a presents a conceptual representation of **A** as a continuous function of time, while the right side of 1a illustrates the temporally discreet sampling of the region at $\boldsymbol{\Delta t}$ intervals. Note that at higher latitudes Δt has several recurring modes and so the picture shown is oversimplified relative to the actual sampling. Fig. 1b illustrates the instantaneous retrieval process of the TRMM satellite. Differences in the swath area of the sensor and the size of the TMI and PR sampling error characteristics are entirely attributed to differences in the swath area. The TMI, moreover, samples at five different frequencies

resulting in five different footprint sizes, which further complicates an accurate assessment of the footprint size.

We can subsequently define the sampling and retrieval errors over **A** by considering a hypothetical scenario consisting of two satellites, one geosynchronous and the other orbiting. The geosynchronous satellite samples **A** continuously and estimates monthly rainfall $\hat{S}_0$, while the orbiting satellite samples **A** intermittently. Based on this measurement scheme, the sampling and retrieval errors for a single month can be estimated with respect to S_0, $\hat{S}_0$ and $\mathbf{R_T}$ as:

$$\xi_{sam} = S_0 - \hat{S}_0, \tag{4a}$$

$$\xi_{ret} = \hat{S}_0 - R_T, \tag{4b}$$

From (4) it can be easily verified that the total error in (2) is simply the sum of $\boldsymbol{\xi}_{\mathbf{ret}}$ and $\boldsymbol{\xi}_{\mathbf{sam}}$. In general, both sampling and retrieval errors contribute appreciably to the total error budget for the month. For a large sample estimates collected over several years, the mean error in the satellite is statistically estimated as:

$$\mathrm{var}(S_0 - R_T) = \mathrm{var}(\xi_{sam} + \xi_{ret}) = \sigma_{sam} + \sigma_{re} + 2\,\mathrm{cov}(\xi_{sam}, \xi_{ret}). \tag{5}$$

In (5), $\boldsymbol{\sigma}_{\mathbf{ret}}$ represents the expectation value for the retrieval error incurred while the satellite is overhead, whereas $\boldsymbol{\sigma}_{\mathbf{sam}}$ represents the expectation value in the sampling error associated with the missing rain information between observations (Laughlin 1981, North 1988). Here it is assumed that the observations are independent and that the measurement error does not depend on when the measurement was made (Laughlin 1981 and Bell and Kundu 2000). Since it is assumed that $\mathbf{S_0}$ and $\mathbf{R_T}$ are uncorrelated, the covariance term in (5) becomes negligible compared to the other two terms. In the next section we will define $\boldsymbol{\sigma}_{\mathbf{sam}}$ **and** $\boldsymbol{\sigma}_{\mathbf{ret}}$ in terms of satellite and ground based rain parameters.

3. Error Separation Methodology

Even if it can be assumed that $\mathbf{R_T}$ is known, there is still not enough information to quantify σ_{sam} and σ_{ret}, because both sources of error become entangled in the total error, defined in terms of the argument defined in (5) as var($S_0 - R_T$). These errors cannot be independently quantified based on simple comparisons between space and ground measurements matched in time and space. The statistical decomposition methodology developed by Fisher (2004, 2007) decouples sampling and retrieval errors estimated on regional scales by generating two monthly rain estimates from a continuous time series of high-resolution ground-based rain measurements. $\mathbf{R_0}$ is the rain rate determined from a continuous integration of the time series in a single month, while $\mathbf{R_S}$ represents the mean monthly rain rate computed by sampling the ground data during times when the satellite is overhead. The size of the grid box used was determined based on the minimum of the satellite product resolution (0.25° x 0.25°).

This methodology assumes that the temporal sampling errors for $\mathbf{S_0}$ and $\mathbf{R_S}$ are equivalent, since both estimates are matched in time and space. The sub-sampled GV estimate effectively introduces an additional degree of freedom used to establish a direct statistical connection between the dual processes of sampling and retrievals.

In performing this type of analysis, the continuous and sub-sampled GV rainfall estimates $\mathbf{R_0}$ and $\mathbf{R_S}$ must first be spatially averaged to the larger grid resolution of the satellite estimates. Mean monthly rain rates are then generated for each month at a spatial scale optimized for the satellite retrievals. Using $\mathbf{R_0}$ and $\mathbf{R_S}$ as validation, we define he sampling and retrieval errors for a single month (ξ_{sam} and ξ_{ret} in terms of the three observables $\mathbf{R_0}$, $\mathbf{R_S}$ and $\mathbf{S_0}$

$$\xi_{sam} = R_S - R_0 \tag{6a}$$

$$\xi_{ret} = S_0 - R_S \tag{6b}$$

Note that the statistically derived parameter $\mathbf{R_S}$ appears in both of the above equations and is effectively linked to both sampling and retrievals.

Assuming that sampling and retrieval errors are uncorrelated (Bell and Kundu 2000 and Fisher 2007), the random errors in the satellite estimate can be approximated as

$$\text{var}(S_0 - R_0) \approx \text{var}(\xi_{sam}) + \text{var}(\xi_{ret}) = \sigma^2_{sam} + \sigma^2_{ret} \tag{7}$$

In this study, $\mathbf{R_0}$ is treated as a best estimate of $\mathbf{R_T}$. Fisher (2007) previously showed that if $\mathbf{R_T}$ replaces $\mathbf{R_0}$, an additional variance term $\boldsymbol{\sigma}_{\mathbf{R0}}$ should be added the right hand side of (7) to account for the errors in the ground data (Fisher 2004, 2007).

The annual and overall sampling and retrieval errors can now be analytically computed year-to-year from the empirical rain parameters, $\mathbf{R_0}$, $\mathbf{R_S}$ and $\mathbf{S_0}$ using (6) and (7) as shown below

$$\sigma_{sam} = \sqrt{\text{var}(\xi_{sam})} = \sqrt{\sigma^2_{R_S} + \sigma^2_{R_0} - 2\text{cov}(R_S, R_0)} \tag{8}$$

$$\sigma_{ret} = \sqrt{\text{var}(\xi_{ret})} = \sqrt{\sigma^2_{s_0} + \sigma^2_{R_S} - 2\text{cov}(S_0, R_S)} \tag{9}$$

In this study, the variances on the right hand side of (8) and (9) were computed relative to the multi-year monthly means determined for each rain parameter from the six-year data period. Previous applications of statistical error decomposition computed errors relative to the annual mean. This modification of the error model reduces the variability around the mean due to seasonal variations in the annual cycle. Here we have not explicitly accounted for errors in the GV data. If $\mathbf{R_0}$ is replaced by $\mathbf{R_T}$ in (7), the definitions of $\boldsymbol{\sigma}_{\mathbf{sam}}$ and $\boldsymbol{\sigma}_{\mathbf{ret}}$ will not be directly affected because these depend on $\mathbf{var(S_0\text{-}R_0)}$. Instead we

need to add an additional term σ_{GV} to account for the variance in $\mathbf{R_0}$ relative to $\mathbf{R_T}$ (Fisher 2007).

An estimation of the sampling and retrieval biases for each sensor provides additional information for evaluating the structure of the error fields and assessing whether the combination of sampling and retrieval biases resulted in an over or underestimation of the long-term rainfall.

Previous applications of this methodology estimated sampling and retrieval biases relative to the corresponding GV references $\mathbf{R_0}$ and $\mathbf{R_S}$ as

$$r_{sb} = \sum_{i=1}^{N} (R_{Si} - R_{0i}) \Big/ \sum_{i=1}^{N} R_{0i} \tag{10}$$

$$r_{rb} = \sum_{i=1}^{N} (S_{0i} - R_{Si}) \Big/ \sum_{i=1}^{N} R_{Si} \, . \tag{11}$$

This bias estimator normalizes the total bias relative to the validation parameter, either $\mathbf{R_0}$ (sampling) or $\mathbf{R_S}$ (retrievals). The summations in the numerator and denominator are computed independently to ensure the stability of $\mathbf{R_S}$, which in some instances can approximate zero.

In this study we will also compute a mean sampling and retrieval bias, defined as

$$m_{sb} = \frac{1}{N} \sum_{i=1}^{N} \left(R_{Si} - R_{0i} \right) \tag{12}$$

$$m_{rb} = \frac{1}{N} \sum_{i=1}^{N} \left(S_{0i} - R_{Si} \right) . \tag{13}$$

The factor N in (11) and (12) corresponds to the total number of 0.25° grid boxes. Sampling and retrieval biases are subsequently estimated using the same factor and is conveniently expressed in units of rain intensity (mm day^{-1} $month^{-1}$), which can be more

directly compared to σ_{sam} and σ_{ret}. Since N also depends on the number of grid boxes in the GV domain for a given data period, the mean bias is not relative to the observations of a particular sensor.

4. Data Description

a. General Overview

Satellite and GV monthly rain estimates for $\mathbf{S_0}$, $\mathbf{R_S}$ and $\mathbf{R_0}$ were spatially matched at 0.25° for all grid boxes with 150 km from the ground radars located at KWAJ and MELB. The top two panels of Fig. 2 display a regional map for each GV site, with concentric range rings shown at 50-kilometer intervals out to 200 km. The lower two panels of Fig. 2 display the land, ocean and coast surface terrain mask for the Goddard Profiling (GPROF) Algorithm (Kummerow et al. 2001) in the estimation of rain rates for the TMI, AMSR-E and the SSM/I. This classification was used to stratify the data so that each classification could be separately analyzed.

b. GV Rain products

The rain parameters $\mathbf{R_0}$ and $\mathbf{R_S}$, as described in the previous section, were computed from the operational TRMM 3A54 and 2A53 GV rain products obtained for KWAJ and MELB. The 3A54 provides a 2x2 km monthly rain map for computing $\mathbf{R_0}$ and the 2A53 provides at 2x2 km instantaneous rain rates, which are used for computing $\mathbf{R_S}$. These rain products are generated by the TRMM Satellite Validation Office and archived and distributed through NASA's Goddard Earth Sciences Data and Information Services Center (GES-DISC). The 3A54 products are derived from the 2A53 by piecewise

integration of the instantaneous rain maps over a one-month period. Contiguous rain maps, however, are only forward integrated up to fifteen minutes. Missing data introduces a potential source of GV uncertainty that is not directly accounted for in this analysis (Wolff et al 2005).

Table 2 shows the number of days per year when the radar was down for more than 4 hours in a day and the mean number of days per month that radar was down. Radar downtime affects the determination of both $\mathbf{R_0}$ and $\mathbf{R_S}$. Radar downtime only affects the estimate of $\mathbf{R_0}$ when it is raining. $\mathbf{R_S}$, on the other hand, is only affected when the satellite is overhead through the number of samples collected in a given month. Since $\mathbf{R_S}$ is based on the unconditional rain rate, the mean will be affected whether it is raining or not. Moreover, because $\mathbf{R_S}$ and $\mathbf{S_0}$ are determined from matching statistics, $\mathbf{S_0}$ is also affected by radar downtime, which reduces the number of observations relative to the total number of overpasses in a month (i.e., there is no matching when the radar is down). Consequently, the number of observations used to compute $\mathbf{R_S}$ and $\mathbf{S_0}$ can never exceed the number of overpasses, but can be systematically lower, which will tend to increase the estimated variances.

Another potential source of error in our analysis relates to not accounting for partial coverage of the grid box by the satellite. In this study, we assumed full coverage, which is not always true, but is a reasonable assumption so long as the satellite observation covers a significant fraction of the grid box. However, the GV radar provides complete coverage for all grid boxes inside of the radar domain. Consequently, the value computed for $\mathbf{R_S}$ and $\mathbf{R_0}$ are always based on 100% coverage of the grid box. Not

accounting for partial coverage in the estimate of $\mathbf{S_0}$, can lead to some mixing of sampling and retrieval errors.

The radar rain rates were estimated out to 150 km using the lowest available Constant Altitude Plan Position Indicator (CAPPI). A CAPPI represents a cross section through the radar volume scan containing multiple tilts (relative to the polar angle). It should be noted that the lowest level CAPPI changes abruptly from 1.5 to 3 kilometers at a distance of 100 km from the radar. MELB has gauges located at all distances within the radar's sampling domain and can account for this jump by relying on the gauge information. KWAJ, however, only has gauges out to about 100 km and so confidence levels in the GV rain estimates at KWAJ are considerably lower beyond 100 km.

c. Satellite rain products

Instantaneous rain rates were obtained for AMSR-E, SSM/I, AMSU-B and the TRMM from orbital track data processed at 0.25° grid-resolution inside of a grid-space that extended out to 150 km. The analysis consists of a 156 grid boxes. The TMI, AMSR-E and SSM/I were each processed using version 6 of the GPROF rain algorithm (Kummerow et al. 2001, Olson et al. 2006). GPROF applies a Bayesian inversion methodology that relates brightness temperature to rain rate by matching observed brightness temperatures to a database of simulated rain profiles constructed from a state of the art cloud-resolving model. AMSU applies the AMSU-B rain rate algorithm developed at NOAA, which infers rain rates from the scattering information in the 89 and 150 GHz channels (Spencer 1989, Weng et al. 2003; Qiu et al. 2005).

The instantaneous rain products were next matched to the ground-based radar estimates during satellite overpass times at 0.25°. The PR rain rates were inferred based

on a determination of an effective reflectivity factor that involves a two-way correction for attenuation through the intervening precipitation observed downward from above the cloud. The attenuation correction represents a significant potential source of error. Another potential source of error involves algorithmic assumptions relating to the drop size distribution. The COM algorithm was developed by Haddad et al (1996) and utilizes the rain information from both the PR and the TMI in the determination of combined rain rate constrained to the sampling region of the PR.

5. Sampling, Retrievals and Climatology

a. KWAJ and MELB: general rain climatology

Climate-scale rain rate observations from orbiting satellites are limited in their ability to accurately resolve quasi-permanent climatic features, such as the diurnal cycle, due to discrete, non-continuous sampling, under-sampling and over-sampling. The systematic coupling of satellite sampling to the regional climatology can introduce additional error variance and bias into the monthly rain estimates (Shin et al. 1990, Bell and Reid 1996, Salby and Callaghan 1997). In this section the effects of climatology on the sampling and retrieval error statistics will be assessed with respect to the diurnal and annual cycle.

b. Diurnal cycle

The rain statistics collected during the month are also sensitive to the mean sampling frequency, the relative sampling intervals between overpasses and the autocorrelation time (Shin and North 1988 and Bell and Kundu 2000). Non-representative sampling of the diurnal cycle can produce systematic errors in the estimation of monthly rainfall, especially for the polar orbiting satellites (Shin et al. 1990,

Bell and Reid 1996, Salby and Callaghan 1997 and McCollum et al. 2002). A single polar orbiting satellite, for example, only collects two observations per day at the same two nominal times and consequently cannot directly observe, even in a statistical sense, the phase and amplitude associated with the mean diurnal cycle. The TRMM satellite, on the other hand, precesses through the diurnal cycle over a characteristic sampling period of about 46 days, which exceeds the time scale over which the observations are integrated (i.e., one month).

A diurnal climatology is displayed in Fig. 3 for KWAJ and MELB using the six years of radar data from the study period. Fig. 3 plots the conditional rain rate as a function of the hour. The conditional mean rain rate provides an indicator of the expected observed rain rate when it is raining and is especially relevant for sun-synchronous satellite orbits. The nominal overpass times for each of the polar orbiting satellites (day and night) are denoted in each panel by symbols superimposed onto this climatology. The phase and amplitude of the diurnal cycles for KWAJ and MELB differ significantly and help to illustrate important differences between the two climate regimes. KWAJ exhibits a low-amplitude diurnal signal, with a small nocturnal maximum characteristic of tropical oceanic rainfall (Wolff and Fisher 2009). The mean hourly rain rate subsequently varies within a narrow range of values. MELB, on the other hand, exhibits a high-amplitude convective phase during the early and late afternoon hours. The difference between the maximum and minimum mean hourly rain rates differ by about 2.0 mm/hr. The polar orbiting satellites obviously are not capable of resolving the diurnal climatology, but non-representative sampling of the diurnal cycle is expected to produce larger sampling errors in the monthly estimates.

Although the satellite orbits tend to be relatively stable, there does exist some long-term drift in the overpass times over the lifetime of each satellite. Figure 4 displays a long-term plot of the equator crossing times for each satellite and shows that the orbital drift varies from satellite to satellite. This drift amounted to about three hours for the three most extreme cases (F14, F15 and N16) over the six-year observation period.

Figure 5 displays the diurnal cycle for KWAJ and MELB as observed by the TRMM satellite and the ground sensors (both continuous and non-continuous sampling). The MELB diurnal cycle was further stratified into ocean, land and coast regimes. The $\mathbf{R_0}$ rain profile displayed in each plot provides the best estimate of the true diurnal climatology (as inferred from six years of rain statistics) and is used to assess differences in the TMI, PR, COM and the sub-sampled estimates $\mathbf{R_{TMI}}$ and $\mathbf{R_{PR}}$ due to temporal sampling errors.

$\mathbf{R_{TMI}}$ and $\mathbf{R_{PR}}$ show very good agreement with the TMI and the PR. They capture both phase and amplitude associated with the observed fine structure. The observed variability in $\mathbf{R_{TMI}}$ and $\mathbf{R_{PR}}$ relative to $\mathbf{R_0}$ is entirely attributed to sampling effects. In the two ocean cases $\mathbf{S_0}$ (i.e., TMI, PR and COM), $\mathbf{R_{TMI}}$ and $\mathbf{R_{PR}}$ exhibit considerable random variability around the $\mathbf{R_0}$ profile. $\mathbf{R_0}$, in contrast, varies smoothly in all four panels of Fig. 5. The pdf of these two oceanic climatologies differ mainly in that a low amplitude maximum occurs in the early morning for KWAJ and the early evening for MELB.

For KWAJ, there exists a low amplitude nocturnal maximum between 4 and 5 am and relative minimum in the late afternoon. MELB, on the other hand, exhibits a small maximum in the early evening around 16 LST. This maximum is coupled with the decaying phase of sea-breeze circulation. By averaging over three hour time-steps, the

random variability relative to $\mathbf{R_0}$ can be further reduced (Negri et al.). It is clear in the MELB Ocean case, however, that additional averaging will not resolve the late afternoon maximum evident in the $\mathbf{R_0}$ climatology, even with additional averaging. Because the MELB profiles are stratified into three distinct cases, there are fewer samples available for each case, which likely accounts for some of additional variability observed in the ocean case. Similarly, the PR and R_{PR} show significantly more variability relative to the TMI and R_{TMI} due to the substantial differences in the PR and TMI swath, which results in fewer samples for the PR.

c. Annual cycle

Whereas sampling errors are modulated by the phase and amplitude of the diurnal cycle, retrieval errors tend to be more sensitive to variations in the annual cycle due to the affects of seasonal changes in the microphysical properties of rainfall. McCollum et al. (2002) observed that microwave rain estimates over the United States tended to overestimate summertime rainfall, while underestimating wintertime rainfall. Fisher (2004, 2007) observed the same tendency for Oklahoma and Central Florida. Similarly, any seasonal changes that affect drop size distributions will have an affect on the PR's measured reflectivity.

Figures 6 and 7 display the annual cycle for KWAJ and MELB for the rain sensors listed in Table 1 using data from the six-year study period. Satellite and GV annual climatologies were determined from monthly rain estimates for $\mathbf{S_0}$, $\mathbf{R_S}$ and $\mathbf{R_0}$. $\mathbf{R_0}$, which is independent of the satellite overpass time, provides an absolute baseline for comparing $\mathbf{S_0}$ and $\mathbf{R_S}$. For MELB, land, ocean and coast climatologies were estimated independently using GROF land, ocean and coast classifications.

KWAJ annual satellite and GV climatologies are shown in Fig. 6. KWAJ receives the bulk of its annual rainfall during the rainy season from about May to November. $\mathbf{S_0}$ and $\mathbf{R_S}$ for each satellite are closely correlated. . For most of the sensors in Fig. 6, $\mathbf{R_S}$ tends to exceed $\mathbf{S_0}$, especially during the rainy season. This trend suggests the existence of a negative retrieval bias relative to the GV radar-inferred estimates. We can see this pattern clearly for the case of the three TRMM rain products shown along the top row of Fig. 6, where there appears to be a substantial retrieval bias during the peak months of the rainy season. The long term mean monthly statistics for $\mathbf{R_0}$ and $\mathbf{R_S}$ are also reasonably well correlated, though there are differences that tend to appear during the peak of the rainy season.

The long-term averages for MELB shown in Fig. 7 reflect differences between the ocean, land and coast cases. MELB-Land and MELB-Coast receive the bulk of the annual rainfall between June and September, whereas MELB-Ocean exhibits an absolute maximum in September during the climatological peak in tropical cyclone and easterly wave activity. A secondary oceanic maximum in June is also observed. Differences between land, coast and ocean are most distinct for AMSR shown in Fig. 7g (these differences also appear in N17, which is not shown). Comparing the MELB $\mathbf{R_0}$-Land and $\mathbf{R_0}$-Coast profiles in Fig. 7i to $\mathbf{S_0}$, all of the satellite sensors tend to overestimate the peak rainfall during June, July and August. It is also interesting to note the differences between the PR and the TMI, for both sensors sample rainfall from the same orbiting platform. The PR tracks closely with $\mathbf{R_S}$ for all three cases, but for the TMI, there appear to be significant retrieval errors over land during the peak rainfall months.

6. Results and Discussion

a. Error Correlation Structure

Scatter diagrams of the satellite estimates of monthly rainfall are used to characterize the sampling ($\mathbf{R_S}$ vs. $\mathbf{R_0}$) and retrieval ($\mathbf{S_0}$ vs. $\mathbf{R_S}$) errors and to evaluate the correlation structure between the estimated and validation parameters. The relevant validation parameters in each case are taken to represent the independent variable: $\mathbf{R_0}$ for the sampling case and $\mathbf{R_S}$ for the retrieval case. The analysis and discussion that follows will ascribe meaning to the correlation coefficients and slope parameters determined from linear regressions of the random variables associated with sampling and retrievals.

1) Sampling

Scatter diagrams of $\mathbf{R_S}$ versus $\mathbf{R_0}$ are presented in Figs. 8 and 9 for KWAJ and MELB for each of the rain sensors. Monthly estimates for MELB were further subdivided into sub-categories corresponding to the GPROF land, ocean and coast surface terrain classifications. Correlation coefficients and slope parameters were calculated for each distribution. These are displayed in Table 4. Sampling errors were estimated by evaluating statistical differences between sub-sampled and continuously sampled GV radar data as described in Section 3.

Table 3 evaluates the sampling frequency for each sensor relative to the average number of overpasses per month for a randomly selected 0.25° grid box inside of 100 km from the GV radar. The Table shows that the TMI and PR collect significantly more samples at MELB than at KWAJ (nearly a factor of 2 difference in number) due to TRMM's lower angle of inclination and its sun-asynchronous orbit. Shin and North (1987) conducted simulations of the TRMM orbit prior to launch and found that TRMM

sampling errors were reduced at higher latitudes due to increased sampling. Their findings are consistent the results of this study.

It is also observed that the polar orbiters collected a few more samples on average over MELB than KWAJ, but this apparent difference is due to reductions in the area of the 0.25° grid box, which varies with latitude due to converging lines of longitude at the poles. F14 was the only sensor with fewer observations over MELB, while over KWAJ its sampling statistics are comparable to the other polar orbiters. This anomaly in the MELB sampling statistics for F14 is therefore probably due to missing overpasses over related to radar downtime.

All the scatter diagrams for KWAJ in Fig. 8 display a similar structure and are characterized by a large range of $\mathbf{R_S}$ values and a much narrower range of $\mathbf{R_0}$ values. Table 4 indicates that $\mathbf{R_S}$ and $\mathbf{R_0}$ are generally not well correlated at the monthly scale, but the degree of correlation is sensitive to differences in the temporal and spatial sampling characteristics of the sensor. For KWAJ, the observed inter-sensor variability depends primary on the relative swath width of the sensor, for near to the equator the satellite sampling frequency is nearly constant for the different satellites analyzed in this study.

Table 4 for KWAJ indicates that the AMSU rain sensors on average exhibited the highest correlation, while the PR/COM group displayed the lowest correlation. This predictable result shows the dependency of the sampling error on the swath geometry of the sensor. AMSU sweeps out a 1600 km swath width compared to a 247 km swath for the PR. It subsequently covers an area 6.5 times larger than the PR per overpass. Slope values for the PMW sensors (excluding PR/COM) range from 0.98 to 1.15. Discrete

temporal sampling results in the satellite tending to overestimate rainfall when $\mathbf{S_0}$ and $\mathbf{R_S}$ are both high, while underestimating rainfall when $\mathbf{S_0}$ and $\mathbf{R_S}$ are very low. Consequently a small number of overestimates at the high end are compensated by a much larger number of underestimates at the low end. Fisher (2004) observed similar results in the long-term PDF of monthly estimates from the TMI and PR collected over Oklahoma. Morrissey and Janowiak (1996) attributed this error correlation structure to a conditional sampling bias in climate-scale estimates resulting from discreet temporal sampling of the satellite. They found that the magnitude and sign of the bias depended on the mean monthly rain rate.

Diagnosing the effects on the MELB results shown in Fig. 9 is more complex due to differences in the land, ocean and coast sub-climate regimes. First examining the polar orbiting PMW sensors, F13 and F14 regress appear to incur negative oceanic sampling biases. This can be inferred from Fig. 9 together with the slope of the regression shown in Table 4. AMSR-E, F15, N15 and N16, on the other hand, appear to incur a positive bias. F13 and F14 were the only two satellites to display lower correlations over MELB than KWAJ. Note F14 was the only satellite to collect fewer observations over MELB. Over land, F14, F15 and N17 are negative, but F13, AMSR-E N15 and N16 are positive. We also observe a significantly larger variance in the both the correlation coefficients and slopes over land, which we attribute to sampling coupled to climate variability associated with the amplitude and phase of the diurnal cycle for the land and coast cases.

The benefits of improved sampling are most clearly observed over MELB for the TRMM rain estimates. The TMI and PR exhibited generally higher correlations and slope values that approach unity for each of the three terrain cases. These improvements are

attributed to both a larger number of observations and more representative sampling of the diurnal cycle.

2) Retrievals

Scatter diagrams of $\mathbf{S_0}$ and $\mathbf{R_S}$ are utilized here to examine retrieval error characteristics. Since both rain parameters are spatio-temporally matched, it is assumed that they observe the same distribution of instantaneous rain rates. Figures 10 and 11 present scatter diagrams of $\mathbf{S_0}$ and $\mathbf{R_S}$ at KWAJ and MELB, respectively, and Table 5 lists the corresponding regression parameters. Table 5 clearly shows that $\mathbf{S_0}$ and $\mathbf{R_S}$ are more highly correlated than $\mathbf{R_S}$ and $\mathbf{R_0}$. The slopes associated with each regression, however, tended to be less than one for both KWAJ and MELB. This observation holds for all the oceanic satellite estimates, again suggesting a positive retrieval bias over the oceans.

The oceanic rain retrievals are of special interest for evaluating the accuracy of the physical rain retrievals of the TMI, AMSR and SSM/I. The oceans provide a cold radiometric surface with a distinguishable polarization signature, allowing for a decoupling of surface emissions from those emanating from the atmosphere above. It should be noted that AMSU-A and B channels lack polarization information and consequently, the lower frequency emission channels on AMSU-A are not used by the AMSU rain rate algorithm, which relies on radiometric information from the 89 and 150 GHz scattering channels on AMSU-B (other lower frequency channels on AMSU-A are used to screen the surface, but only play an ancillary role in the determination of the rain rate).

The correlation coefficients for the rain retrievals over KWAJ and MELB-Ocean are restricted to a similar range of values. Correlations for KWAJ range from 0.66 (F15) to 0.91 (PR/COM), while for MELB-Ocean they range from 0.64 (F13) to 0.88 (TMI). Slope values determined from each regression are also consistently less than one for all of the rain sensors, revealing the presence of a negative oceanic retrieval bias. The retrieval bias will be considered more quantitatively in the Section 7b.

For the TMI, AMSR and SSM/I, differences in the error correlation for the ocean can be related to differences in the relative size of the FOV in the emission channels. The FOV for the TMI and AMSR water vapor channels, for example, are about 450 km^2 and 560 km^2, respectively, and cover an area smaller than the area of the grid box (~750 km^2). The SSM/I nominal FOV for the water vapor channel is about 2000 km^2 and more closely approximates the size of a 0.50 grid box (~3000 km^2).

The larger footprint also introduces additional beam-filling effects that are significant when sampling highly convective systems with large rain rate gradients embedded in the rain field (Kummerow et al. 1998). Oceanic SSM/I rain retrievals showed lower correlations and higher variance than TMI and AMSR for both KWAJ and MELB-Ocean. These differences in the error correlations structure to first order are attributed to the relative differences in the size of the FOV with respect to the gridding scale of the study.

Rain retrievals over land and coast are evaluated using MELB-Land and MELB-Coast displayed in Fig. 11. The GPROF land and coast algorithm is constrained by the observations in the high frequency channels, corresponding to the two 85.5 GHz channels on the TMI and SSM/I and the 89 GHz channels on AMSR. These channels have a

smaller FOV than the lower frequency channels, eg., 35 km^2 at 85.5 GHz compared to 400 km^2 in the water vapor channel at 21.3GHz. The better resolution provides some structural information on the rain rate gradients associated with convective systems, but this information must be ascertained from the ice scattering signature that occurs in higher regions of the cloud.

Correlations varied over a larger range and appear related to size differences in the relative sensor FOVs. Over land, correlations range from 0.53 (N17) to 0.90 (COM), whereas and over coast they range from 0.45 (N17) to 0.92 (COM). Relative differences in the slope parameters more closely correspond to differences in the relative land, ocean and coast climatology and the overpass times of the polar orbiting satellites.

Although AMSU has an additional high frequency channel at 150 GHz, the AMSU group in general exhibited the lowest correlations over land and coast. AMSU scatter diagrams suggest problems in observing higher instantaneous rain rates, which may explain some of the large negative differences between $\mathbf{S_0}$ and $\mathbf{R_S}$**.** The AMSU ice scattering algorithm may also have ancillary problems screening out surface anomalies. The SSM/I group exhibits the most variability amongst the PMW sensors. The TMI/AMSR group exhibits significantly higher correlations over the ocean than over land and coast due to the addition of the low frequency rain information.

The PR/COM retrieval statistics showed the best overall performance relative to correlation slope and also reveal a higher range of values. The PR/COM statistical indexes also show more relatively consistency in the retrievals over land, ocean and coast scenes. The PR has much better vertical resolution than the PMW rain sensors and because it has a smaller FOV can better resolve strong gradients in the rain field

associated with smaller scale convective rain structures. Still, the surface classification can impact the reflectivity measurement of the PR, either due to changes in the drop size distribution over land and ocean (assumptions about the DSD assumptions are built into the algorithm) or to the surface reference technique applied by the PR algorithm (Meneghini et al 2000, Iguchi et al. 2000, Robertson et al. 2003).

b. Geo-spatial Distribution of Errors and Biases

1) Sampling errors and biases

KWAJ and MELB climate-scale rain estimates were analyzed at the 0.25° grid spacing using the error model described in Section 3. All mean error statistics were computed inside of 100 km to avoid mixing GV rain estimates computed from different CAPPI levels. Mean sampling errors for KWAJ are shown in Table 6 and ranged from 3.1 to 6.3 mm/day. Oceanic sampling errors for MELB spanned a lower range of values from 2.4 to 4.8 mm/day, about 25% less than the range estimated for KWAJ. Table 6 also suggests that for MELB sampling and retrieval errors over land are greater than over ocean.

Differences in the oceanic sampling errors determined for KWAJ and MELB are correlated with increased satellite sampling rates at higher latitudes. Examining Table 3, we see that for the TMI and the PR the sampling rate increases by nearly a factor of 2 due to the satellite's lower angle of inclination (Shin and North 1988). For the other PMW sensors, the number of overpasses does not increase but the grid boxes at higher latitudes are smaller due converging line of longitude, resulting in broader coverage of the grid box at higher latitudes.

The geo-spatial distributions of the sampling errors for KWAJ and MELB are shown in Figs. 12 and 14, respectively. Inside of 100 km, the KWAJ sampling errors for PMW rain sensors are confined to a relatively small range of variability. Sampling errors tend to increase beyond this range, but inside of 100 km we do not see a clear connection between the distribution of sampling errors and the timing of the overpass. Comparing the six panels for MELB, we observe considerable inter-sensor variability. Differences between land, ocean and coast are evident in some of the panels but there is no clear pattern that clearly separates the sampling errors associated with the geo-terrain mask.

The PR's sampling errors exhibited the greatest range of variability at both sites. Table 6 indicates that these errors are about 1/3 greater than the TMI as seen in Table 6. Based on the mean sampling statistics listed in Table 3, the PR only collects about half as many samples over KWAJ than for MELB. These large sampling errors limit the relative accuracy of the PR's climate-scale rain estimates, even though as we will see, its rain retrievals outperform the other sensors. The PR rain estimates also not as sensitive to the surface classification.

Mean sampling biases for KWAJ shown in Table 7a ranged from 0.35 to 1.03 mm day^{-1} and were systematically positive for all the PMW sensors. Ocean biases for MELB were also systematically positive overall, ranging from -0.48 to 0.49. For MELB, only N16 (-0.48) and F15 (-0.04) exhibited an overall negative sampling bias. F15 and the PR/COM exhibited the lowest long-term sampling bias for KWAJ (0.35). PR/COM biases shown in Fig. 13 are more randomly distributed, whereas the other PMW sensors over KWAJ are systematically positive across the entire GV domain.

A stronger coupling between the sampling times and the land-coast-ocean MELB climatology produces a more complex bias pattern for MELB shown in Fig. 15 than what was observed for KWAJ in Fig. 13. In Fig. 15 there exists considerable inter and intra-sensor variability. The inferred biases for the two AMSU sensors in Fig. 15, N15 biases are mostly positive while N17 biases are mostly negative. From Fig. 3, it is tempting to attribute this striking pattern to differences in the timing of the overpasses. N17, for instance, does not sample the convective cycle shown Fig. 3 for MELB, whereas the daytime overpass for N15 flies over MELB at about 18 LST. AMSR-E flies over MELB at 1:30 LST during the peak of the convective cycle, resulting in predominantly positive sampling biases across the GV sampling domain. The sign of the biases for F13, on the other hand, tends to change based on the geo-terrain classification (positive over land, negative over ocean). The sampling biases for the two TRMM sensors tended to be lower and more randomly distributed than the other PMW sensors, as further evidenced by the mean biases for each (0.10 mm/day for the TMI and 0.17 for the PR) .

2) Retrieval errors and biases

Bulk retrieval errors for KWAJ are shown in Table 6 and span a range between 2.1 and 3.7 mm hr^{-1}. At the low end of this range is the TMI/AMSR group (2.1 mm hr^{-1}), whereas the SSM/I group is found at the high end (3.7 mm hr^{-1}). MELB-Ocean exhibited a slightly lower trend (1.7 to 3.3 mm hr^{-1}), but we also observe more intra-group variability within each sensor class. This section will focus on the sensor characteristics and algorithmic differences in the retrievals to explain the observed errors and biases.

The geo-spatial distribution of retrieval errors for KWAJ and MELB are displayed in Figs. 16 and 18. The COM replaces N17 in the top right panel of each figure. The retrievals errors for KWAJ tend to be isotropically distributed, with significantly larger errors observed at distances greater than 100 from the radar. Increases in the retrieval errors outside of 100 km are attributed to greater uncertainties in the GV radar estimates due to the sudden shift from the 1.5 to 3.0 km CAPPI. This shift in CAPPI levels was previously described in Section 4. At KWAJ there is no gauge information beyond 80 km to calibrate rain rates estimated from the 3.0 km CAPPI. Although there is some residual range dependency observed at MELB as well where gauge stations exist out to 150 km, range effects probably contribute less to the variability than other factors such as differences in surface terrain (Note since there exists no gauge information over the Atlantic Ocean east of the GV radar, oceanic rain rates must be calibrated using the gauge PDF over land).

Mean retrieval biases for KWAJ and MELB are shown in Table 7b. All of the oceanic rain estimates for KWAJ exhibit large biases ranging from -1.93 to -0.93 mm/day. The geo-spatial distribution of biases shown in Fig. 17 shows a relatively homogenous distribution of negative retrieval biases throughout the GV domain, with some tendency for larger biases in the far southern quadrant. Oceanic retrieval biases for MELB also tended to be negatively skewed, but occur within a lower range (-0.92 to 0.08). The geo-spatial distribution of biases for PMW sensors shown in Fig. 19 shows a strong dependency on the terrain type and the coupling of the satellite orbit to the sampling of the climatology.

Negative oceanic retrieval biases for TMI, AMSR and SSM/I are partly attributed to beam filling in the low frequency emission channels and partly attributed to saturation of the channels at high rain rates (Ha and North 1994, Kummerow 1998). Beam filling tends to smear the peak rain rates of the smaller convective cells over the whole FOV. Saturation places unphysical constraints on the maximum observable rain rate. AMSU oceanic rain rates on the other hand are determined using a pure scattering algorithm that only utilizes high frequency rain information and consequently are less correlated with the integrated water content at the cloud base. The PR has the smallest FOV of all the sensors examined and is better suited for detecting the peak rain rates associated with small-scale convective cells, but the PR also has to account for the two-way attenuation due to the intervening water and ice in the observed cloud system (Meneghini, 2000).

The mean oceanic sampling and retrieval biases in Table 7a and 7b tend to exhibit opposite signs. This same pattern is also observed in Figs. 13, 15, 17 and 19 for both KWAJ and MELB, which effectively reduces the overall bias in the rain estimate. As noted in Section 4, it is expected that there will be some mixing of sampling and retrieval biases due to the fact $\mathbf{R_S}$ always fills the entire grid box, while $\mathbf{S_0}$ does not necessarily fill the box, we do not consider this an explanation for the differences observed. Error mixing in this case should be a random effect that should lead to increased variability – through under and over estimates relative to a correctly weighted $\mathbf{S_0}$ – but should not have a large effect on the long-term mean statistics. Consequently, we relate differences in the sampling and retrieval biases to fundamental differences in the structure of the sampling and retrieval distributions characterized in the scatter diagrams shown in Figs. 8-11.

MELB retrieval errors characterized in Table 6 tended to increase appreciably over land and coast relative to ocean when compared to the results computed for each sensor. TMI/AMSR bulk errors for MELB are nearly the same over the ocean, but the TMI retrieval errors over land and coast were considerably lower than AMSR. The TMI and AMSR have similar instrument characteristics and determine rain rates using the GPROF rain algorithm. We subsequently relate the more salient differences over land and coast to increased variability in the diurnal rain rate statistics for AMSR due to differences in the sampling times of each satellite. AMSR flies over MELB at approximately 0130 and 1330 LST each day, where TRMM precesses through the diurnal cycle at different times. AMSR is subsequently more likely to observe higher convective rain rates during the early afternoon overpass. Similar reasoning can be applied to explain intra-group differences observed for SSM/I and AMSU.

More salient inter- and intra-sensor differences in the satellite retrievals appear in the bias fields for MELB shown in Fig. 19. N15 tends to exhibit positive retrieval biases over land and negative biases over the ocean. These two bias "regimes" are partitioned according to the location of the Florida coastline. F13, in contrast, displays a large swath of positive coastal biases that straddle the Florida coastline. This same pattern was observed in F14 and F15 as well (but this data was only available through 2006). We attribute this distinguishable feature to factors associated with the instrument characteristics and larger FOV of the SSM/I, and not to differences in overpass times.

7. Conclusions

Regional sampling and retrieval errors in monthly rainfall were statistically estimated for five different microwave sensors on board eight orbiting satellites using six-

years of instantaneous satellite rain measurements collected over Kwajalein and Melbourne, Florida. Instantaneous ground-based radar rain estimates were used to sub-sample the data during satellite overpasses to decouple the sampling and retrieval errors from the total monthly error budget as described in Section 3.

Satellite and GV climatologies constructed from the data sets showed that the satellite rain estimates were highly correlated with GV rain estimates sub-sampled during satellite overpasses, and GV sub-sampled rain estimates, moreover, resolved most of the fine structure observed in the satellite climatologies. This empirical methodology, however, will tend to overestimate the satellite sampling error due to intermittent radar downtime at times when the satellite is overhead by reducing the effective number of matching overpasses relative to actual number of times the satellite flies over the site. Radar downtime, however, should not affect the assessment of the retrieval errors. Furthermore, the quantitative assessment of satellite sampling errors still provides a relative measure for evaluating the different sampling designs and provides an absolute baseline for assessing the impact of sampling errors on the long-term rain estimates.

Long-term sampling errors, as expected, were closely linked to the swath area of the rain sensor and the sampling frequency of the satellite, while sampling biases were more closely associated with the coupling of the sampling times to the diurnal climatology associated with each GV site. The TRMM satellite orbit collected more samples over MELB than KWAJ, which resulted in a significant reduction in the TMI and PR sampling errors over MELB Ocean relative to KWAJ. The polar orbiting satellites also showed some reduction in the sampling errors over MELB Ocean due in part to a ~13% reduction in the area of the 0.25° grid box at the higher latitude. For

evaluating oceanic rainfall trends, the relative benefits of the TRMM orbit in reducing random sampling errors and biases were marginal compared to the polar orbiting satellites.

The TRMM sensors, however, did show lower sampling biases over MELB Land and Coast where the diurnal cycle exhibits a large amplitude during the afternoon hours. For these two cases, the two TRMM sensors provided significantly less biased rainfall estimates due to TRMM's asynchronous orbit. For the polar orbiting sensors, the sampling biases over Land and Coast were mixed and were sensitive to the overpass times relative to the phase of the diurnal cycle. The benefits of the TRMM sampling design were much less clear over oceanic surfaces, where a low amplitude diurnal cycle prevailed. Overall, positive long-term sampling biases were observed at KWAJ for all of the sensors, and similarly, positive oceanic sampling biases were observed for most of the sensors at MELB.

All of the rain estimates tended to exhibit negative retrieval errors over ocean surfaces by between 10 and 30% relative to the two GV radars. This important result was observed over both KWAJ (all ocean) and MELB Ocean and appears to be a significant issue for the algorithm developers. Inter-sensor differences in the retrieval biases were most prominent for MELB where there exists a strong coupling between the diurnal cycle and the satellite sampling times. This study did not attempt to quantify seasonal variations in the error characteristics, but direct comparisons of satellite and GV annual climatologies, along with previous studies by McCollum et al. (2002) and Fisher (2007), suggest that the PMW rain algorithms may not be adequately handling seasonal changes in the microphysical properties of rainfall.

The SSM/I, TMI and AMSR-E monthly rain retrievals utilize both emission and scattering channels over ocean surfaces, whereas AMSU only utilizes high frequency scattering channels, which are less correlated with surface rainfall. Based on satellite comparisons with the GV oceanic estimates, SSMI/I, TMI and AMSR-E, tended to yield higher correlations with ground estimates relative to AMSU. Results from the error analysis were somewhat mixed but the TMI/AMSR-E group did tend to exhibit smaller retrieval errors over ocean.

The PR/COM group exhibited the highest correlations with the ground-based radars and the rain retrievals were less dependent on the characteristics of the surface classification. Although the PR outperformed most of the PMW rain sensors, its poor sampling statistics limits its potential for monitoring long-term rainfall trends. However, as can be seen from an examination of the error and bias characteristics of the COM, he PR provides important rain information for improving the rainfall estimates associated with the microwave retrievals and for diagnosing the internal structure of individual rain systems.

References

Bell T. L., and N. Reid, 1993: Detecting the Diurnal Cycle of Rainfall Using Satellite Observations. *J. Appl. Meteor.*, **32,** 311-322**.**

Bell T. L., and P. K. Kundu, 2000: Dependence of satellite sampling error on monthly averaged rain rates: comparison of simple models and recent studies. *J. Appl. Meteor*., **13**, 449-462.

Bell, T. L., P. K. Kundu, and C. D. Kummerow, 2001: Sampling errors of SSM/I and TRMM rainfall averages: comparison with error estimates from surface data. *J. Appl. Meteor*., **40**, 938-954.

Fisher, B. L., 2007: Statistical error decomposition of regional-scale climatological precipitation estimates from the Tropical Rainfall Measuring Mission (TRMM*). J. Appl. Meteor. and Climatol.*, **46**, 791-813.

Fisher, B. L., 2004: Climatological validation of TRMM TMI and PR monthly rain products over Oklahoma. *J. Appl. Meteor*., **43**, 519-535.

40, 1801-1820.

Ha, E.,, and G. R. North, 1995: Model studies of the beam-filling error for rain-rate retrieval with microwave radiometers. *J. Appl. Meteor*., **12**, 268-281.

Haddad, Z., E. Im, S. L. Durden, and S. Henly, 1996: Stochastic filtering of rain profiles using radar, surface-referenced radar, or combined radar-radiometer measurements. *J. Appl. Meteor.*, **35**, 229-242.

Kongoli, C., R. R. Ferraro, P. Pellegrino, H. Meng and C. Dean, 2007: The utilization of the AMSU high frequency measurements for improved coastal rain retrievals. Geophys. Res. Lett., 34, L17809, doi:10.1029/2007GL029940.

Kummerow, C.W., and Coauthors, 2001: The evolution of the Goddard Profiling Algorithm (GPROF) for rainfall estimation from Passive Microwave Sensors. *J. Appl. Meteor*., **40**, 1801-1820.

Kummerow, C. W. Barnes, T. Kozu, J. Shiue, J. Simpson, 1998: The tropical rainfall measuring mission (TRMM) sensor package. *J. Atmos. Oceanic Technol*., **15**, 809-817.

Laughlin, C. R., 1981: On the effect of temporal sampling on the observation of mean rainfall. *Precipitation Measurements from Space*, D. Atlas and O. Thiele, Eds., NASA Publication, D59-D66.

McCollum, J. R., W. F. Krajewski, R. R. Ferraro, M. B. Ba, 2002: Evaluation of biases of satellite rainfall estimation algorithms over the continental United States, *J. Appl. Meteor*., **41**, 1065-1080.

McConnell, A., and G. North, 1987: Sampling errors in satellite estimates of tropical rain. *J. Geophys. Res.*, **92**, 9567-9570.

Meneghini, R., T. Iguchi, T. Kozu, L. Liao, K. Okamoto, J. A. Jones, J., Kwiatkowski, 2000: Use of the surface reference technique for path attenuation estimates from the TRMM precipitation radar. *J. Appl. Meteor*., **39**, 2053-2070.

Morrissey, M. L., and J. E. Janowiak, 1996: Sampling-induced conditional biases in satellite climate-scale rainfall estimates, *J. Appl. Meteor.*, **35**, 541-548.

Negri, A., J., T. L. Bell and L. Xu, 2002: Sampling of the Diurnal Cycle. *J. Appl. Meteor*., **19**, 1333-1344.

North, G .R., 1988: Survey of sampling problems for TRMM. Tropical Rainfall Measurements, J. S. Theon and N. Fugono, A. Deepak Publ., 337-348.

Oki, R., and A. Sumi, 1994: Sampling simulation of TRMM rainfall estimation using radar-AMeDAS composites. J Appl. Meteor., 33, 1597-1608.

Olson, W. S., and Co-authors, 2006: Precipitation and latent heating distributions from satellite passive microwave radiometry. Part I: Improved method and uncertainty estimates. *J. Appl. Meteor*., 702-720.

Qiu, S., P. Pellegrino, R. Ferraro, and L. Zhao, 2005: The improved AMSU rain-rate algorithm and its evaluation for a cool season event in the western United States. Wea. Forecasting, **20**, 761–774.

Robertson, F. R., D. E. Fizjarrald, C. D. Kummerow, 2003: Effects of uncertainty in TRMM precipitation radar path integrated attenuation on interannual variations of tropical oceanic rainfall. *Geophys. Res. Lett.,* **30**, 50 doi: 10.1029/2002GL016416.

Salby M. L., and P. Callaghan. 1997: Sampling error in climate properties derived from satellite measurements: consequences of undersampled diurnal variability. *J. Climate*, **10**, 18-36.

Shin, K., and G. R. North, 1988: Sampling error study for rainfall estimate by satellite using a stochastic model. *J. Appl. Meteor.*, **27**, 1218-1231.

Shin, K., G. R. North, Y. Ahn, and P. A. Arkin, 1990: Times scales and variability of area-averaged tropical oceanic rainfall. *J. Appl. Meteor*., **118**, 1507-1516.

Spencer, R. W., H. M. Goodman, and R. E. Hood, 1989: Precipitation retrieval over land and ocean with the SSM/I. Part I: Identification and characteristics of the scattering signal. *J. Atmos. Ocean. Tech*., **6**, 254-273.

Steiner, M. T. L. Bell, Y. Zhang and E. F. Wood, 2003: Comparison of two methods for estimating the sampling-related uncertainty of satellite rainfall averages based on a large radar dataset. *Journal of Climate*, **16**, 3759–3778.

Weng, F., L. Zhao, R. Ferraro, G. Poe, X. Li, and N. Grody, 2003: Advanced Microwave Sounding Unit cloud and precipitation algorithms. *Radio Sci.,* **38**, 8068-8079.

Wilheit, T. T., 1988: Error analysis for the Tropical Rainfall Measuring Mission (TRMM). *Tropical Rainfall Measurements*, J. S. Theon and N. Fugono, Eds., A. Deepak Publishing, 377-385.

Wolff, D. B., and B. L. Fisher, 2009: Assessing the relative performance of microwave-based satellite rain-rate retrievals using TRMM ground validation data. *J. Appl. Meteor*., **48**, 1069-1099.

Wolff, D. B., D. A. Marks, E. Amitai, D. S. Silberstein, B. L. Fisher, A. Tokay, J. Wang, and J. L. Pippitt, 2005: Ground validation for the Tropical Rainfall Measuring Mission (TRMM). *J. Atmos. Oceanic Technol*., **22**, 365-380.

Wright, Tom, 2006: Tropical storm Talas formation and impacts at Kwajalein Atoll, *27th Conf. on Hurricanes and Tropical Meteor.*, J16A.3.

TABLE CAPTIONS

TABLE 1 Instrument and orbital characteristics for the eight satellites and five rain sensors used in the study.

TABLE 2. Radar Downtime.

TABLE 3. Mean Sampling Frequency per Month.

TABLE 4. Correlations coefficients and slopes of linear regressions characterizing the relationship between $\mathbf{R_S}$ and $\mathbf{R_0}$

TABLE 5. Correlations coefficients and slopes of linear regressions characterizing the relationship between $\mathbf{S_0}$ and $\mathbf{R_S}$

TABLE 6. Summary sampling and retrieval error statistics for KWAJ and MELB stratified by the GPROF surface terrain classification (land, ocean or coast).

TABLE 7a. Sampling bias statistics for KWAJ and MELB.

TABLE 7b. Retrieval bias statistics for KWAJ and MELB.

FIGURE CAPTIONS

Fig. 1. The top half the figure a) illustrates the process of discrete temporal sampling. The left side of 1a) represents the entire spatio-temporal domain of the sampled region A. The right side of 1a) shows the sequence of discrete snapshots collected at overpasses separated by time intervals, Δt. The lower half of the figure 1b) illustrates the retrieval process for the TRMM satellite. The TMI and PR retrieve rainfall information from area A for the region defined by the swath of each sensor. The footprint of each sensor subsequently determines the resolution of the measurement. Although the TMI and PR both obtain snapshots of A at Δt, the PR incurs larger sampling errors due to differences in the area of the swath.

Fig. 2 Top two panels display site maps for KWAJ (top left) and MELB (top right). Range rings are shown out to 200 km. Rain gauge locations are also shown. The lower two panels display the GPROF surface terrain mask for KWAJ (lower left) and MELB (lower right)

Fig 3 Mean diurnal cycle for KWAJ (top) and MELB (bottom) computed during the study period as a function of the hour. Each polar orbiting satellite is represented by a unique symbol shown in the legend showing the two times when the satellite flies over the GV site.

FIG. 4 Equator crossing times during the lifetime of the satellites analyzed in the study. The dotted vertical lines enclose the study period from 2003 to 2008. The row of times shown at the bottom of the figure represents the total temporal drift during the study period.

Fig 5 Diurnal rain climatology for KWAJ and MELB estimated for the six-year study period using the TRMM rain products (TMI, PR and COM). The four panels compare rain profiles for $\mathbf{S_0}$, $\mathbf{R_S}$ and $\mathbf{R_0}$. Each profile has been normalized based on the total rainfall over the 24-hour period.

FIG. 6 Annual rain climatology for KWAJ inferred from six-year study period for (a) TMI, (b) PR, (c) COM, (d) F13, (e) F14, (f) F15, (e) AMSR, (i) N15 and (j) N17. Each panel provides profiles for $\mathbf{S_0}$, $\mathbf{R_S}$ and $\mathbf{R_0}$.

FIG. 7 Annual rain climatology for MELB inferred from six-year study period for for (a) TMI, (b) PR, (c) COM, (d) F13, (e) F14, (f) F15, (e) AMSR, (i) N15 and (j) R_0. The lower right panel (j) represents the true rain climatology based on $\mathbf{R_0}$ as stratified by land, ocean and coast. The other panels represent the inferred climatology based on the $\mathbf{S_0}$ and $\mathbf{R_S}$, which have been further stratified based on the surface criteria.

FIG. 8 Scatter plots for KWAJ computed at 0.25° inter-comparing R_S and R_0 monthly estimates.

FIG. 9 Scatter plots for MELB computed at 0.25° inter-comparing R_S and R_0 monthly estimates land (solid line, open circles), ocean (dash-dot line, triangles) and coast (dashed line, plus sign) cases.

FIG. 10 Scatter plots for KWAJ computed at 0.25° inter-comparing S_0 and R_S monthly estimates.

FIG. 11 Scatter plots for MELB computed at 0.25° inter-comparing S_0 and R_S monthly estimates for the land (solid line, open circles), ocean (dash-dot line, triangles) and coast (dashed line, plus sign) cases.

FIG. 12 Geographical distribution of sampling errors in mm day^{-1} for KWAJ considered for the entire study period (2003-2008).

FIG. 13 Geographical distribution of sampling biases for KWAJ considered for the entire study period (2003-2008).

FIG. 14 Geographical distribution of sampling errors for MELB in mm day^{-1} considered for the entire study period (2003-2008).

FIG. 15 Geographical distribution of sampling biases for MELB considered for the entire study period (2003-2008).

FIG. 16 Geographical distribution of retrieval errors for KWAJ in mm day^{-1} considered for the entire study period (2003-2008).

FIG. 17 Geographical distribution of retrieval biases for KWAJ considered for the entire study period (2003-2008).

FIG. 18 Geographical distribution of retrieval errors for MELB in mm day^{-1} considered for the entire study period (2003-2008).

FIG. 19 Geographical distribution of retrieval biases for MELB considered for the entire study period (2003-2008).

TABLE 1. Instrument and orbital characteristics for the eight satellites and five rain sensors used in the study.

Satellite	Agency Sponsor	Sensor Type	Launch (Yr/Mon)	No. Chan.	Freq. Range (GHz)	Swath Width (Km)	Altitude (Km)
F13	DMPS	SSM/I	1997/03	7	19-85.5	1400	830
F14	DMPS	SSM/I	1997/05	7	19-85.5	1400	830
F15	DMPS	SSM/I	1999/12	7	19-85.5	1400	830
N15	NOAA	AMSU-B	1998/05	5	89 – 183	1600	830
N16	NOAA	AMSU-B	2000/09	5	89 – 183	1600	830
N17	NOAA	AMSU-B	2002/06	5	89 – 183	1600	830
Aqua	NASA	AMSR-E	2002/05	12	6.9 – 89	1445	705
TRMM	NASA	TMI	1997/11	9	10 – 85.5	759	402
TRMM	NASA	PR	1997/11	N/A	13.8*	215	402
TRMM	NASA	COM	1997/11	N/A	TMI/PR^	215	402

* Active precipitation radar

^Hybrid rain product that combines the rain information from the TMI and PR.

TABLE 2. Radar Downtime

	KWAJ		MELB	
Year	Radar down for more than 4 hours in day (days/year)	Mean Radar down time (days/month)	Radar down for more than 4 hours in day (days/year)	Mean Radar down time (days/month)
2003	32	2.7	12	1.0
2004	36	3.0	56	4.7
2005	19	1.6	34	5.7*
2006	26	2.2	48	4.0*
2007	18	1.5	42	3.5
2008	11	0.9	11	1.2*

* averages computed based on fewer than 12 months

TABLE 3. Mean Sampling Frequency per Month.

	Mean Sampling Frequency (Samples/Month)	
Satellite	**KWAJ**	**MELB**
F13	30.5	32
F14	28	24
F15	29	32
N15	45	49
N16	49	53
N17	45	49
AMSR	31	35
TMI	34	62
PR	10.5	19
COM	10.5	19

TABLE 4. Correlations coefficients and slopes of linear regressions characterizing the relationship between $\mathbf{R_S}$ and $\mathbf{R_0}$

Satellite	KWAJ		MELB					
	Ocean		Land		Ocean		Coast	
	Cor.	Slope	Cor.	Slope	Cor.	Slope	Cor.	Slope
F13	0.49	0.98	0.55	1.14	0.36	0.56	0.44	0.97
F14	0.48	1.07	0.29	0.47	0.45	0.69	0.33	0.62
F15	0.47	1.00	0.31	0.51	0.71	1.10	0.51	0.88
N15	0.60	1.03	0.69	1.40	0.74	1.05	0.67	1.11
N16	0.67	1.15	0.76	1.53	0.77	1.03	0.70	1.29
N17	0.60	1.00	0.53	0.55	0.76	1.14	0.62	0.70
AMSR	0.55	1.03	0.52	1.35	0.58	1.12	0.60	1.37
TMI	0.52	0.98	0.63	1.01	0.78	1.12	0.67	1.06
PR/COM	0.30	0.88	0.39	0.98	0.48	1.08	0.44	0.97

TABLE 5. Correlations coefficients and slopes of linear regressions characterizing the relationship between S_0 and R_S

Satellite	KWAJ		MELB					
	Ocean		Land		Ocean		Coast	
	Cor.	Slope	Cor.	Slope	Cor.	Slope	Cor.	Slope
F13	0.71	0.71	0.66	0.86	0.68	0.68	0.90	0.90
F14	0.70	0.70	0.66	0.89	0.70	0.81	0.74	1.42
F15	0.66	0.69	0.63	0.60	0.73	0.80	0.69	0.93
N15	0.74	0.66	0.69	0.86	0.68	0.67	0.56	0.68
N16	0.75	0.64	0.56	0.68	0.74	0.70	0.66	0.61
N17	0.71	0.56	0.53	0.68	0.53	0.68	0.45	0.63
AMSR	0.87	0.71	0.74	0.72	0.88	0.72	0.78	0.79
TMI	0.87	0.77	0.81	1.04	0.88	0.72	0.78	0.75
PR	0.91	0.75	0.88	0.72	0.86	0.88	0.90	0.78
COM	0.91	0.69	0.90	1.06	0.83	0.95	0.92	0.96

TABLE 6. Summary sampling and retrieval error statistics for KWAJ and MELB stratified by the GPROF surface terrain classification (land, ocean or coast).

Satellite	Sampling Errors (mm/day)				Retrieval Errors (mm/day)			
	KWAJ	MELB			KWAJ	MELB		
	Ocean	Land	Ocean	Coast	Ocean	Land	Ocean	Coast
F13	4.1	3.9	3.6	3.5	3.5	4.0	2.9	4.4
F14	4.4	3.4	3.4	4.1	3.7	3.5	3.0	4.7
F15	4.3	2.9	2.8	3.2	3.7	2.6	2.6	3.0
N15	3.4	3.4	2.4	2.7	2.8	4.0	2.7	3.4
N16	3.1	3.3	2.5	3.1	2.8	2.9	2.6	3.0
N17	3.2	2.0	2.6	2.2	2.8	3.4	3.3	2.4
AMSR	3.9	4.2	3.3	3.8	2.1	3.6	2.0	3.2
TMI	4.0	2.9	2.4	2.7	2.1	2.6	1.7	2.3
PR	6.3	5.0	4.8	4.3	2.7	2.4	2.8	2.0
COM	6.3	5.0	4.8	4.3	2.7	2.7	3.2	2.0

TABLE 7a: Sampling bias statistics for KWAJ and MELB.

Satellite	Sampling Biases							
	KWAJ				MELB			
	Ocean		Land		Ocean		Coast	
	r_{sb}	m_{sb}	r_{sb}	m_{sb}	r_{sb}	m_{sb}	r_{sb}	m_{sb}
F13	0.10	0.49	0.22	0.68	0.05	0.17	0.02	0.05
F14	0.15	0.71	-0.25	-0.81	0.04	0.12	-0.15	-0.45
F15	0.07	0.35	-0.22	-0.69	-0.01	-0.04	-0.12	-0.35
N15	0.21	0.97	0.42	1.31	0.12	0.38	0.18	0.54
N16	0.22	1.03	0.17	0.51	-0.15	-0.48	0.09	0.25
N17	0.12	0.56	-0.35	-1.09	0.00	0.01	-0.26	-0.77
AMSR	0.17	0.79	0.20	0.61	0.09	0.28	0.25	0.73
TMI	0.17	0.77	0.03	0.10	0.07	0.24	0.06	0.18
PR	0.08	0.35	0.06	0.18	0.15	0.49	-0.05	-0.15
COM	0.08	0.35	0.06	0.18	0.15	0.49	-0.05	-0.15

TABLE 7b: Retrieval bias statistics for KWAJ and MELB

Satellite	Retrieval Biases							
	KWAJ				MELB			
	Ocean		Land		Ocean		Coast	
	r_{rb}	m_{rb}	r_{rb}	m_{rb}	r_{rb}	m_{rb}	r_{rb}	m_{rb}
F13	-0.29	-1.47	0.18	0.68	-0.11	-0.40	0.48	1.48
F14	-0.33	-1.83	0.14	0.34	-0.18	-0.61	0.67	1.73
F15	-0.37	-1.93	0.12	0.29	-0.05	-0.17	0.48	1.27
N15	-0.24	-1.34	0.15	0.68	-0.10	-0.38	0.00	0.01
N16	-0.32	-1.82	-0.09	-0.35	-0.21	-0.58	-0.19	-0.63
N17	-0.31	-1.61	-0.20	-0.41	-0.28	-0.92	-0.42	-0.93
AMSR	-0.24	-1.32	-0.02	-0.07	-0.08	-0.27	-0.07	-0.25
TMI	-0.23	-1.24	0.13	0.43	-0.13	-0.45	-0.13	-0.41
PR	-0.29	-1.46	-0.08	-0.26	-0.10	-0.36	-0.07	-0.26
COM	-0.18	-0.93	0.23	0.75	0.02	0.08	0.17	0.48

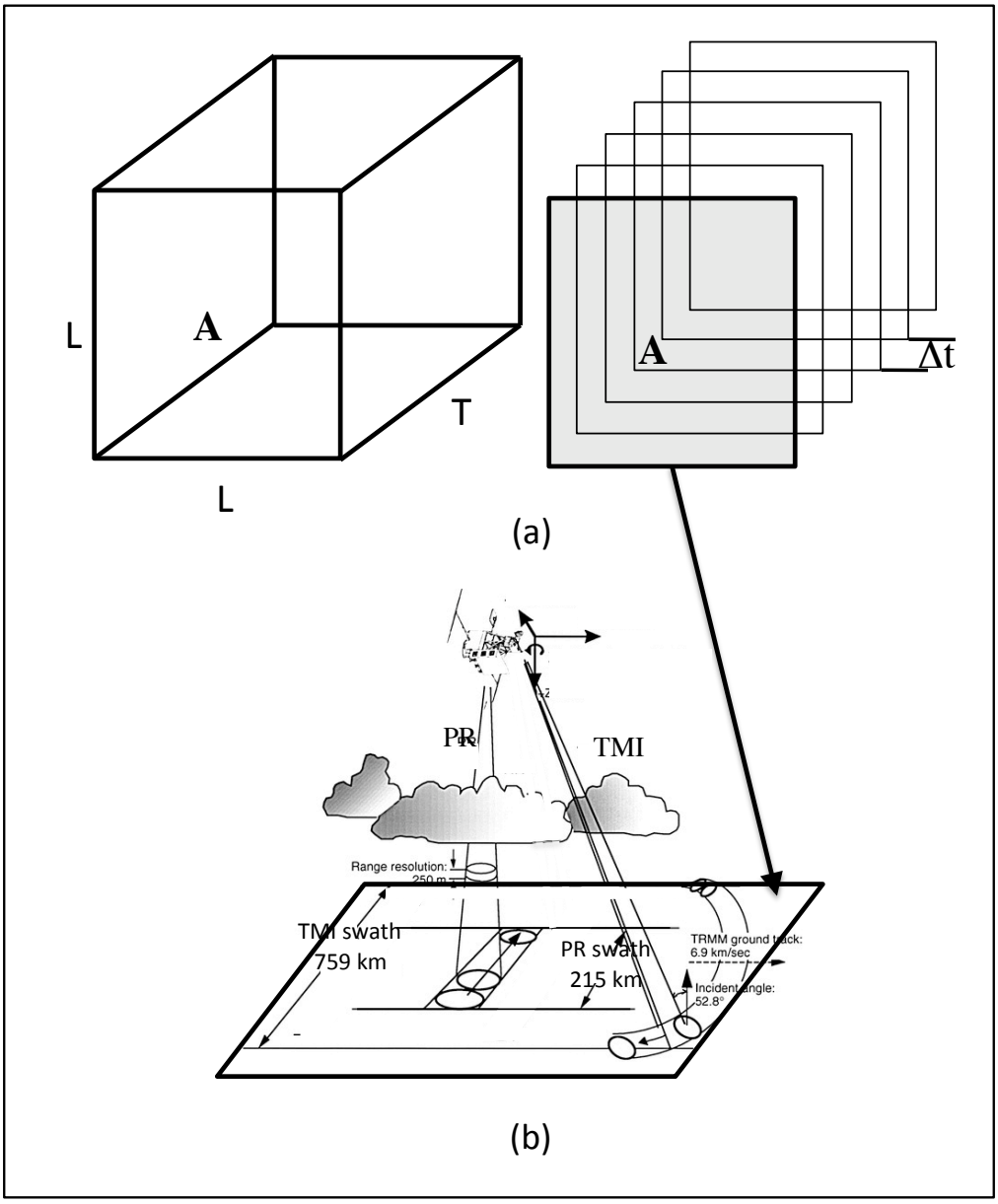

Fig. 1. The top half the figure a) illustrates the process of discrete temporal sampling. The left side of 1a) represents the entire spatio-temporal domain of the sampled region A. The right side of 1a) shows the sequence of discrete snapshots collected at overpasses separated by time intervals, Δt. The lower half of the figure 1b) illustrates the retrieval process for the TRMM satellite. The TMI and PR retrieve rainfall information from area A for the region defined by the swath of each sensor. The footprint of each sensor subsequently determines the resolution of the measurement. Although the TMI and PR both obtain snapshots of A at Δt, the PR incurs larger sampling errors due to differences in the area of the swath.

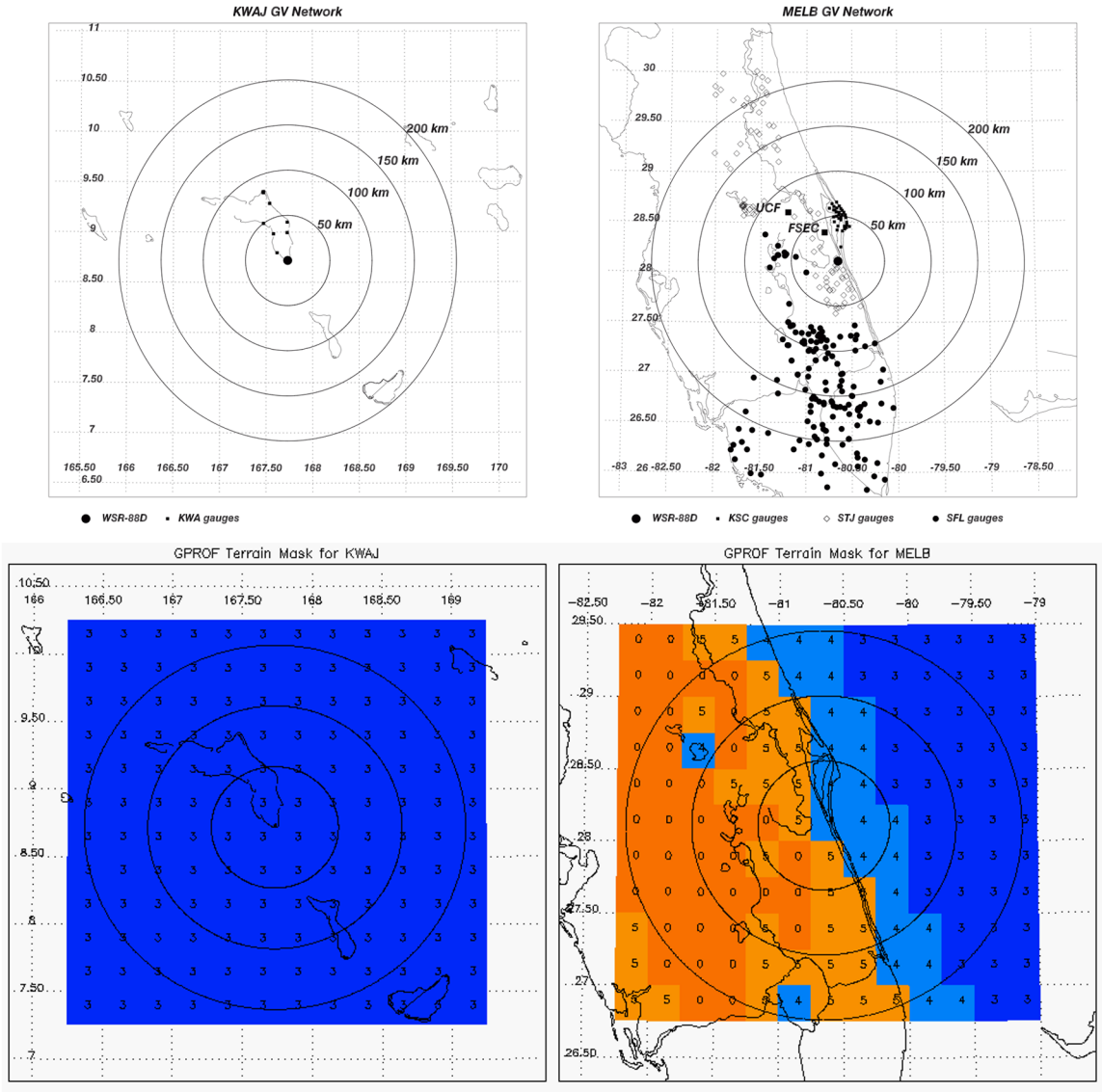

Fig. 2 Top two panels display site maps for KWAJ (top left) and MELB (top right). Range rings are shown out to 200 km. Rain gauge locations are also shown. The lower two panels display the GPROF surface terrain mask for KWAJ (lower left) and MELB (lower right)

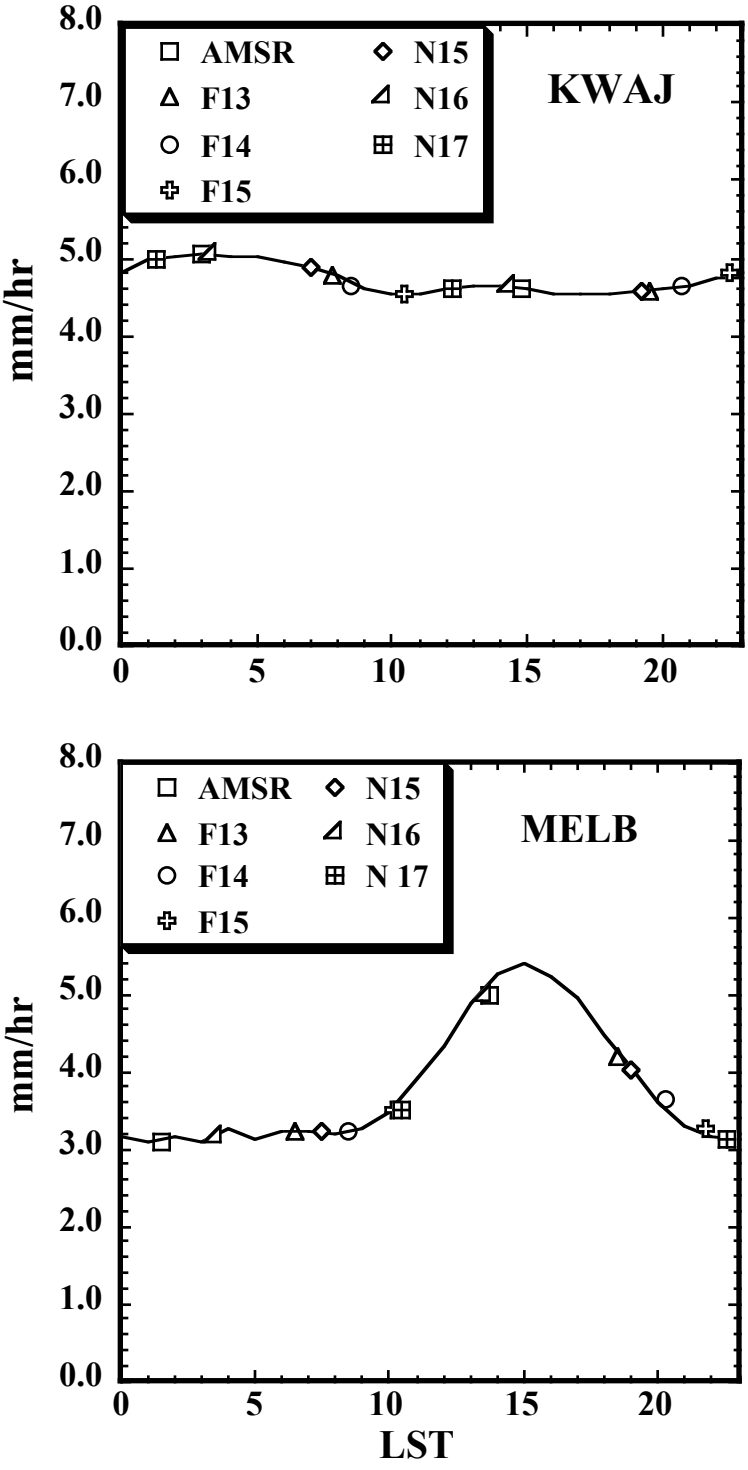

Fig 3 Mean diurnal cycle for KWAJ (top) and MELB (bottom) computed during the study period as a function of the hour. Each polar orbiting satellite is represented by a unique symbol shown in the legend showing the two times when the satellite flies over the GV site.

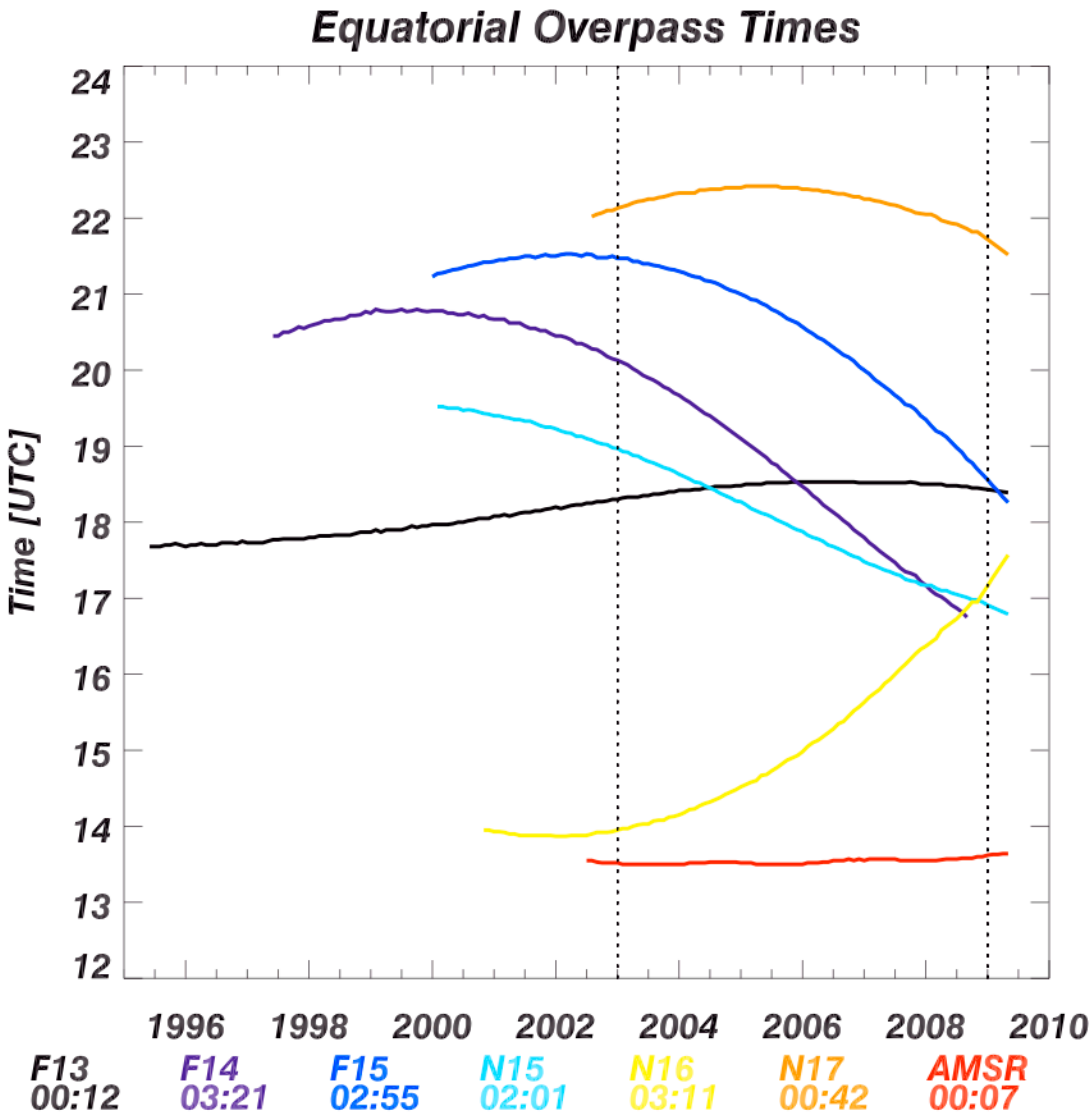

Fig 4 Equator crossing times during the lifetime of the satellites analyzed in the study. The dotted vertical lines enclose the study period from 2003 to 2008. The row of times displayed at the bottom of the figure represents the total temporal drift during the study period.

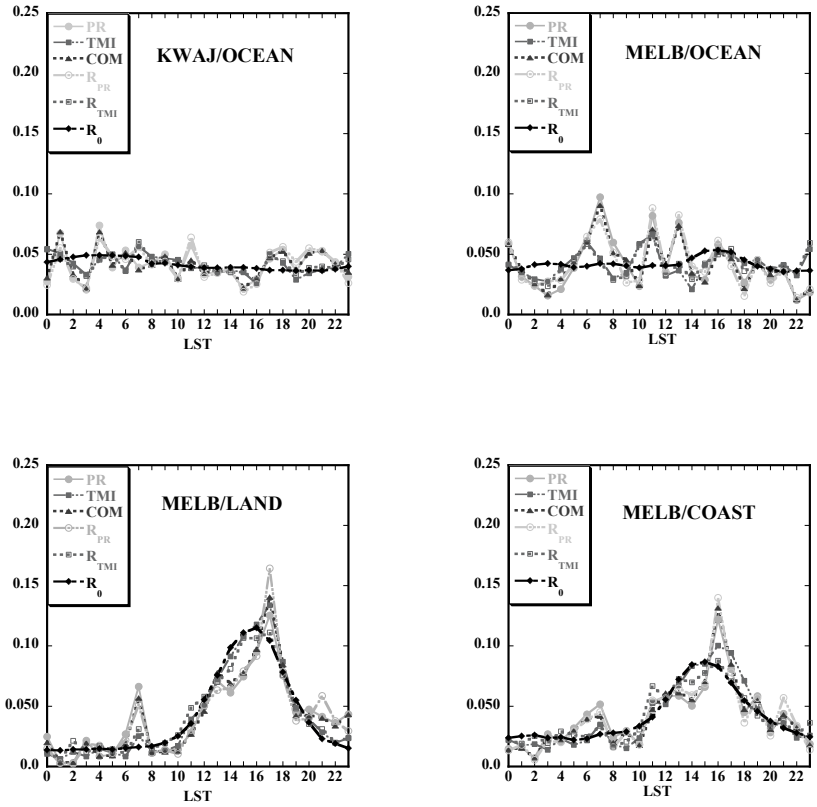

Fig 5 Diurnal rain climatology for KWAJ and MELB estimated for the six-year study period using the TRMM rain products (TMI, PR and COM). The four panels compare rain profiles for $\mathbf{S_0}$, $\mathbf{R_S}$ and $\mathbf{R_0}$. Each profile has been normalized based on the total rainfall over the 24-hour period.

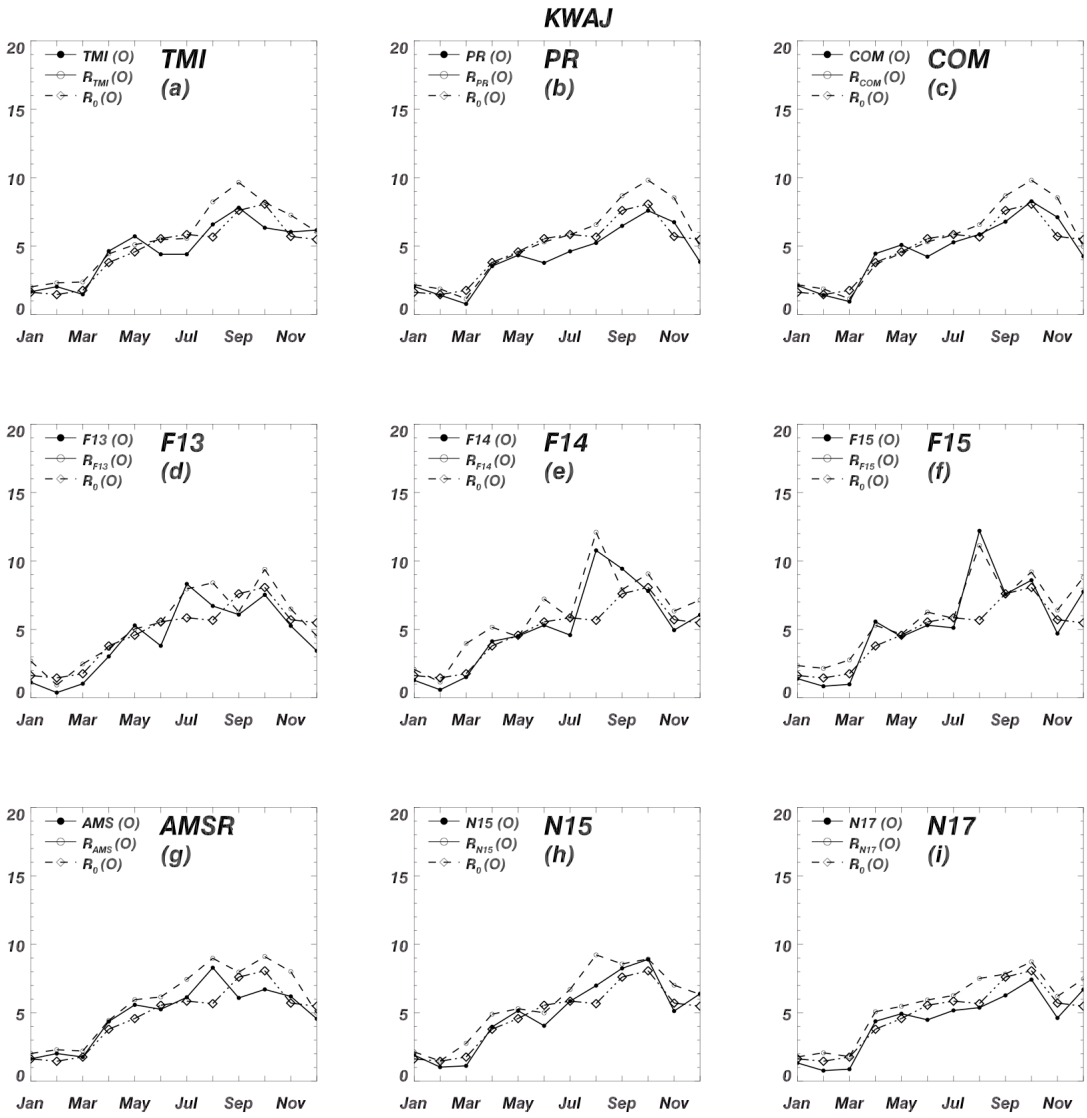

Fig 6 Annual rain climatology for KWAJ inferred from six-year study period for (a) TMI, (b) PR, (c) COM, (d) F13, (e) F14, (f) F15, (e) AMSR, (i) N15 and (j) N17. Each panel provides profiles for $\mathbf{S_0}$, $\mathbf{R_S}$ and $\mathbf{R_0}$.

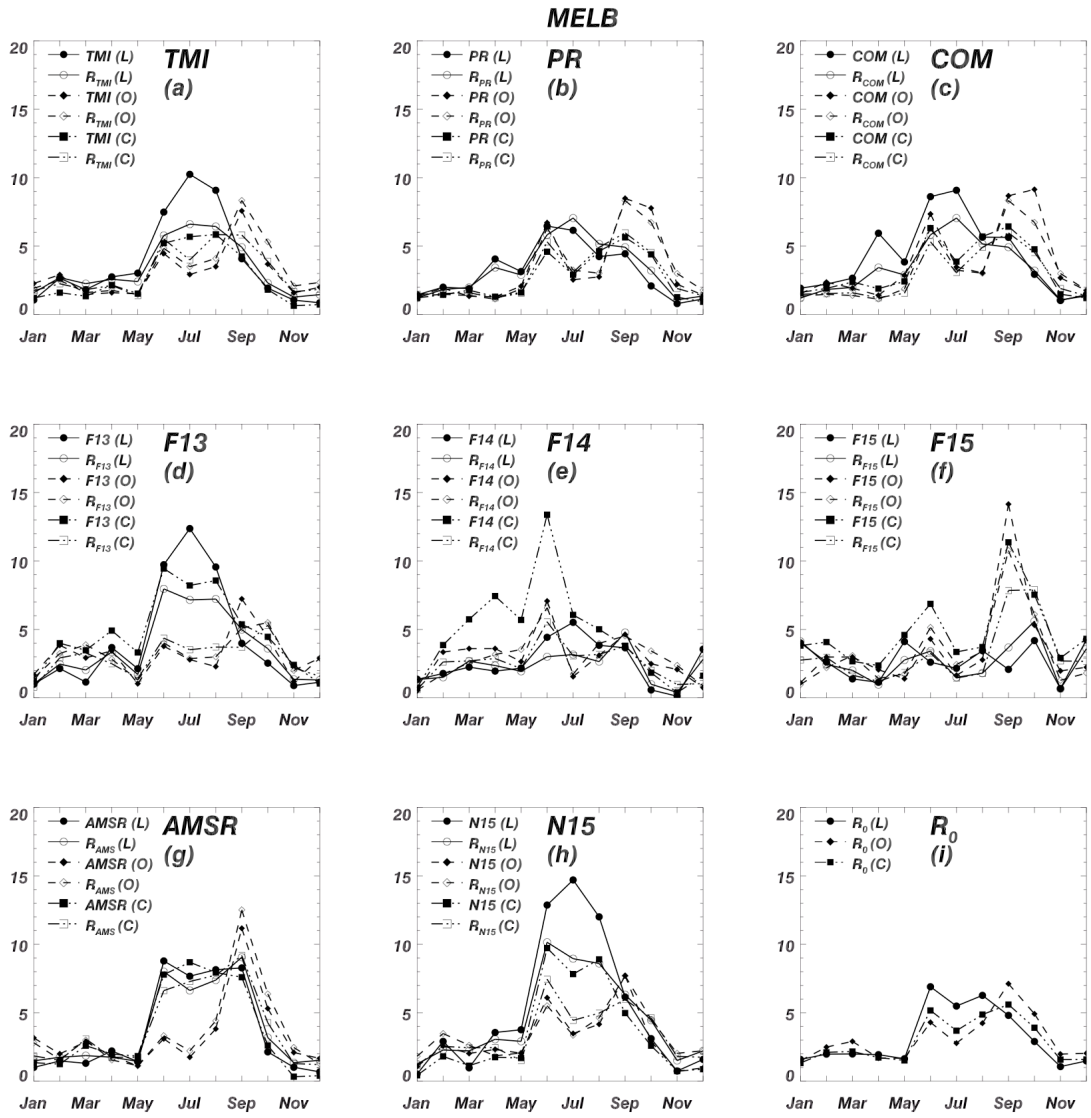

Fig 7 Annual rain climatology for MELB inferred from six-year study period for for (a) TMI, (b) PR, (c) COM, (d) F13, (e) F14, (f) F15, (e) AMSR, (i) N15 and (j) R_0. The lower right panel (j) represents the true rain climatology based on $\mathbf{R_0}$ as stratified by land, ocean and coast. The other panels represent the inferred climatology based on the $\mathbf{S_0}$ and $\mathbf{R_S}$, which have been further stratified based on the surface criteria.

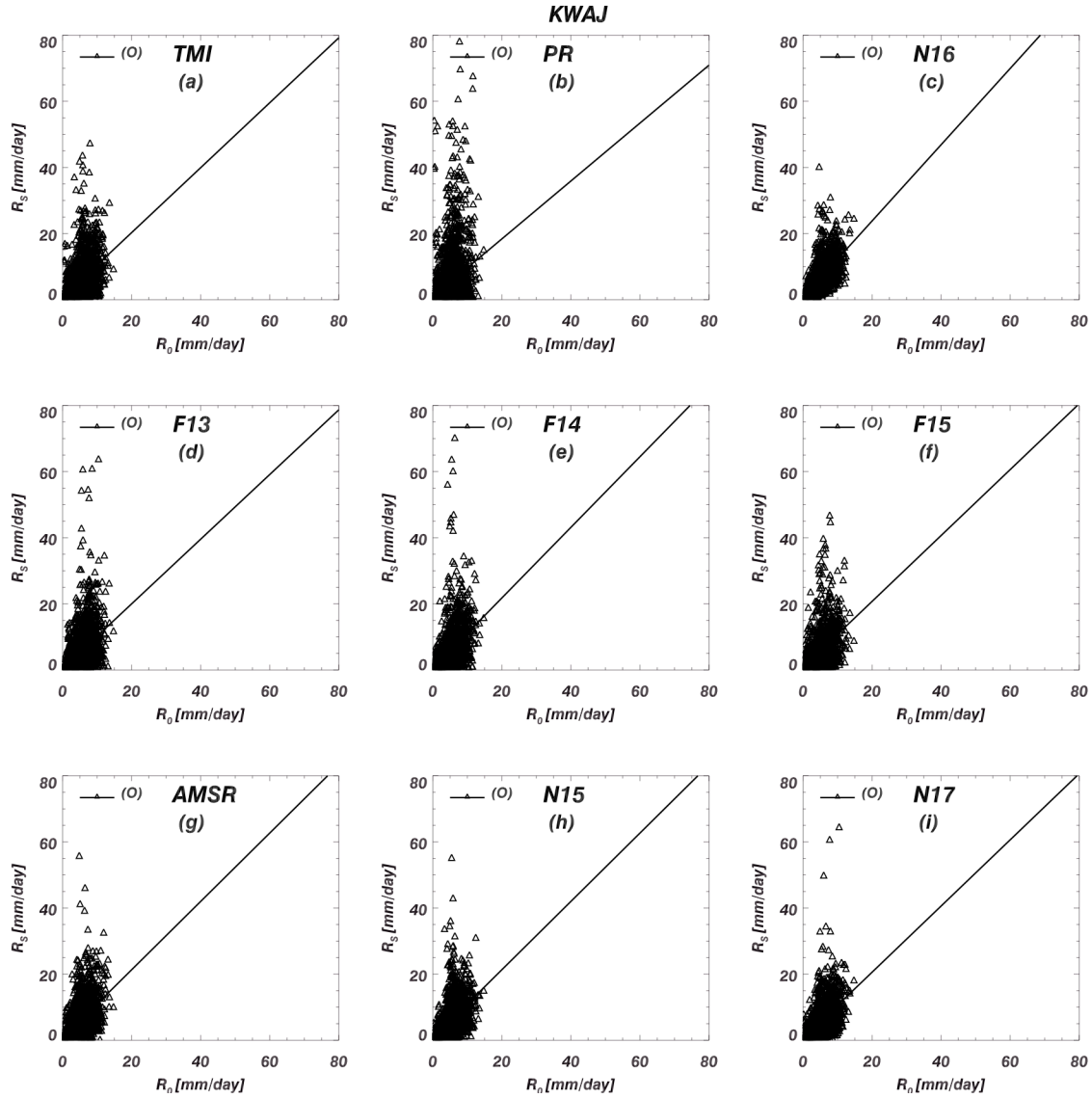

Fig 8 Scatter plots for KWAJ computed at 0.25° inter-comparing R_S and R_0 monthly estimates.

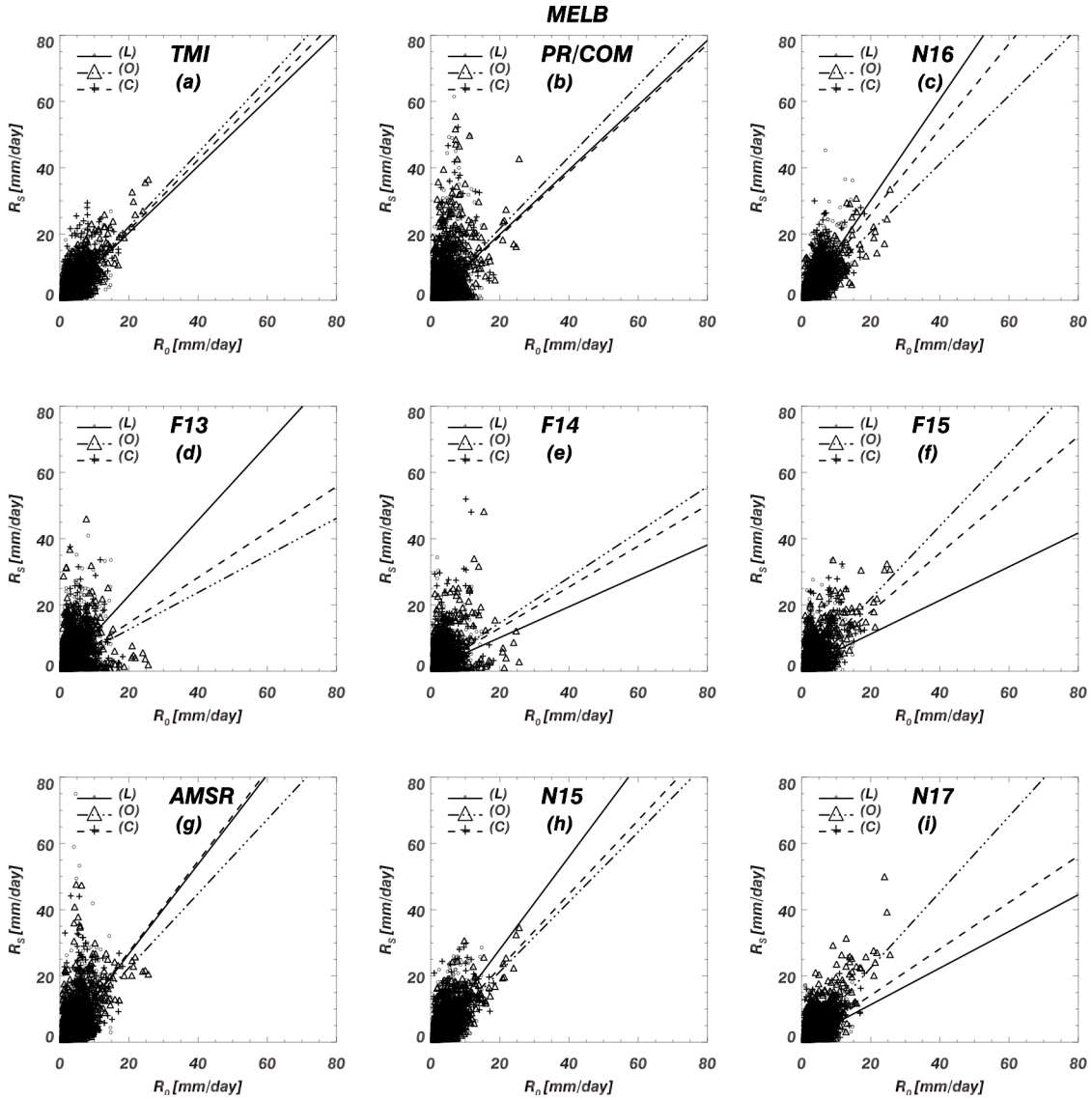

Fig 9 Scatter plots for MELB computed at 0.25° inter-comparing R_S and R_0 monthly estimates land (solid line, open circles), ocean (dash-dot line, triangles) and coast (dashed line, plus sign) cases.

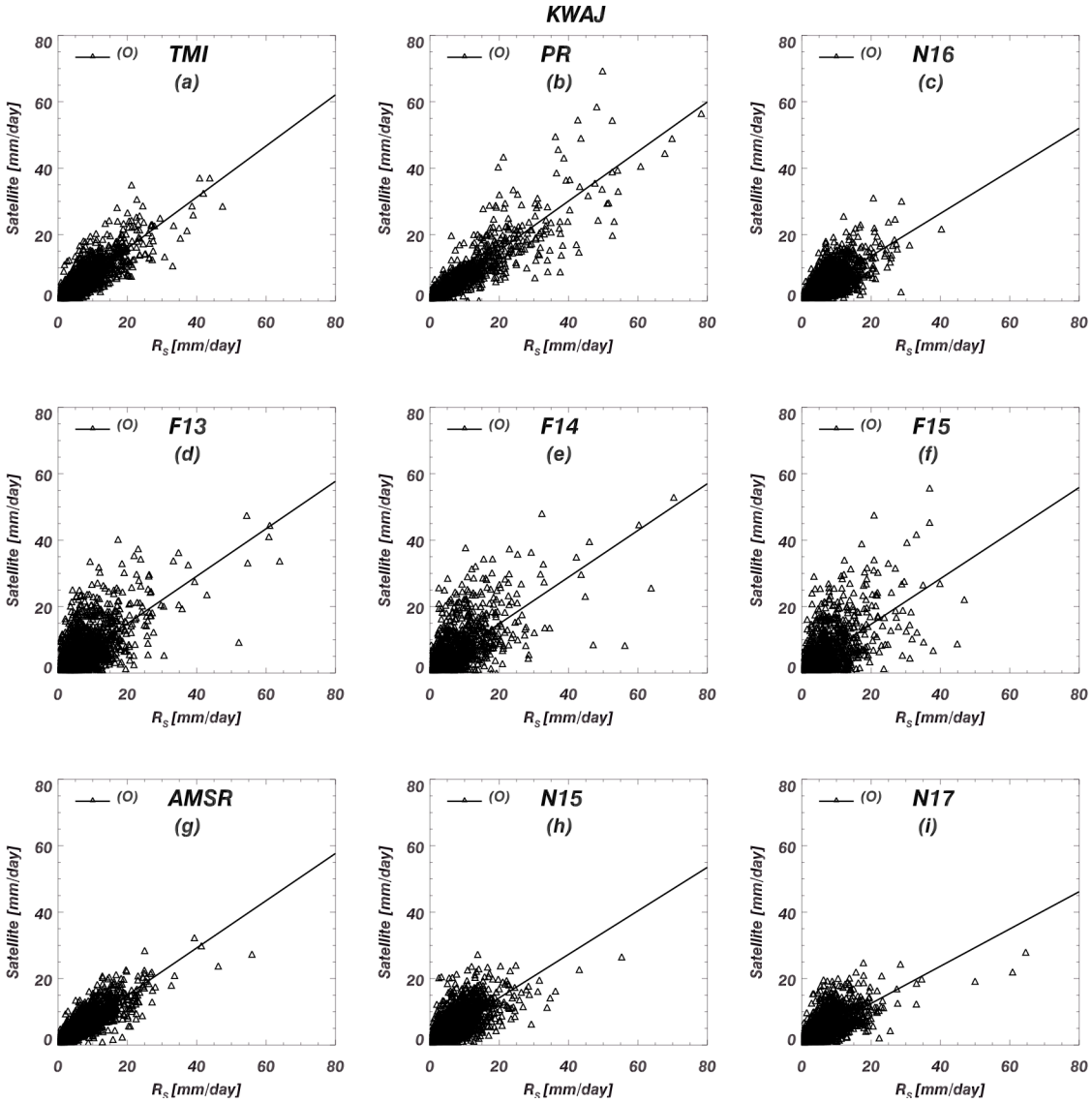

Fig 10 Scatter plots for KWAJ computed at 0.25° inter-comparing S_0 and R_S monthly estimates.

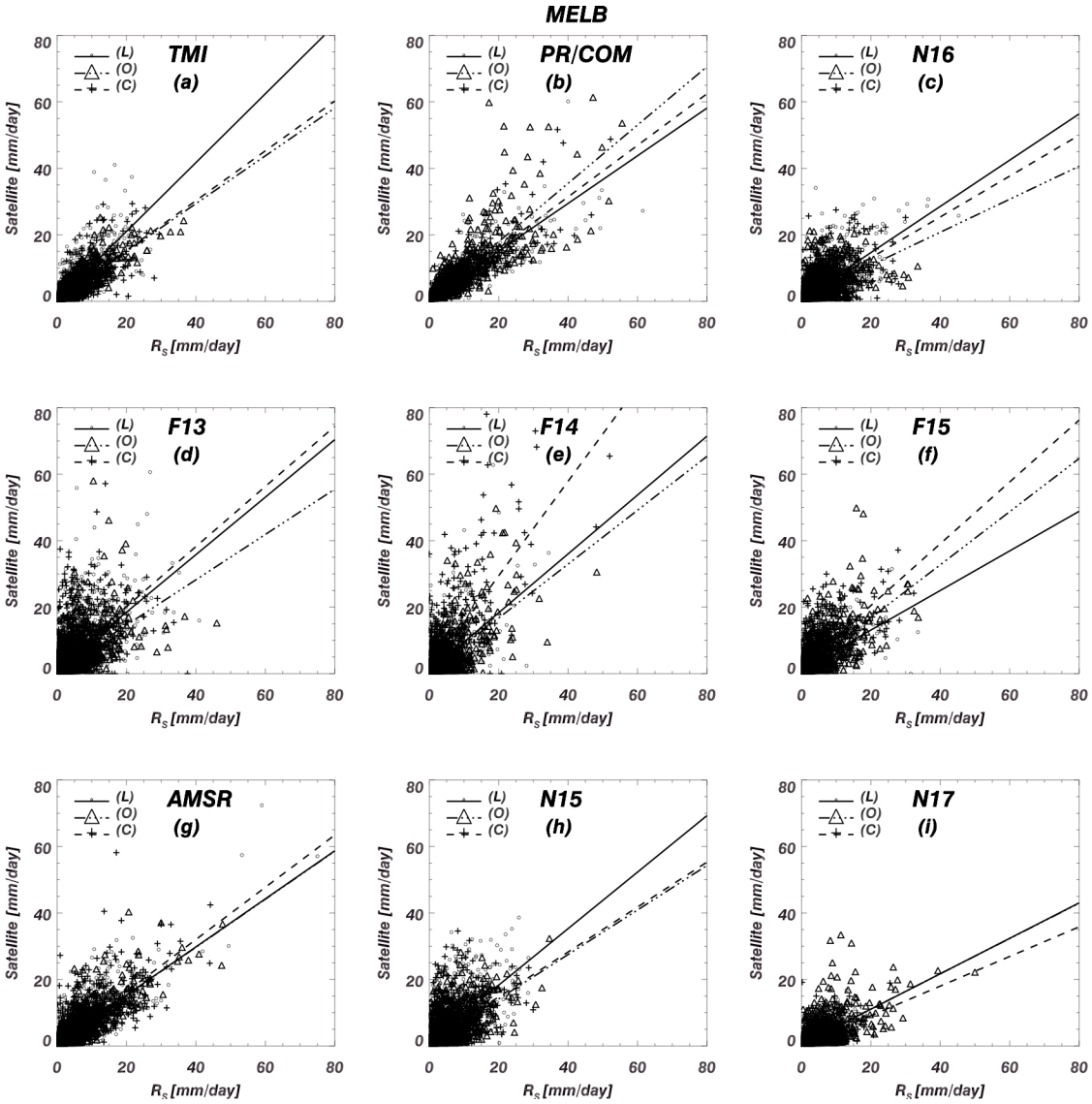

Fig 11 Scatter plots for MELB computed at 0.25° inter-comparing S_0 and R_S monthly estimates for the land (solid line, open circles), ocean (dash-dot line, triangles) and coast (dashed line, plus sign) cases.

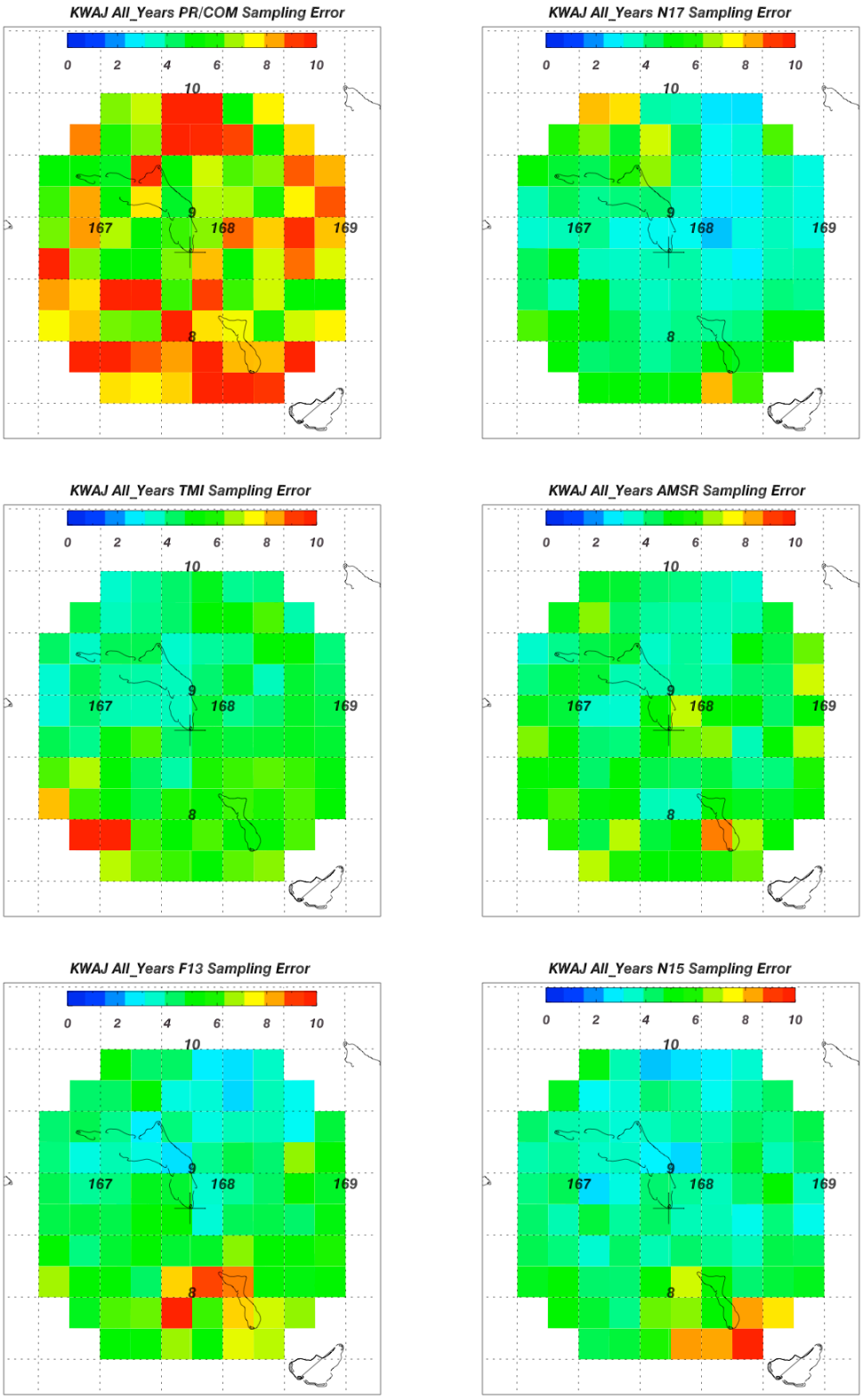

Fig 12 Geographical distribution of sampling errors in mm day^{-1} for KWAJ considered for the entire study period (2003-2008).

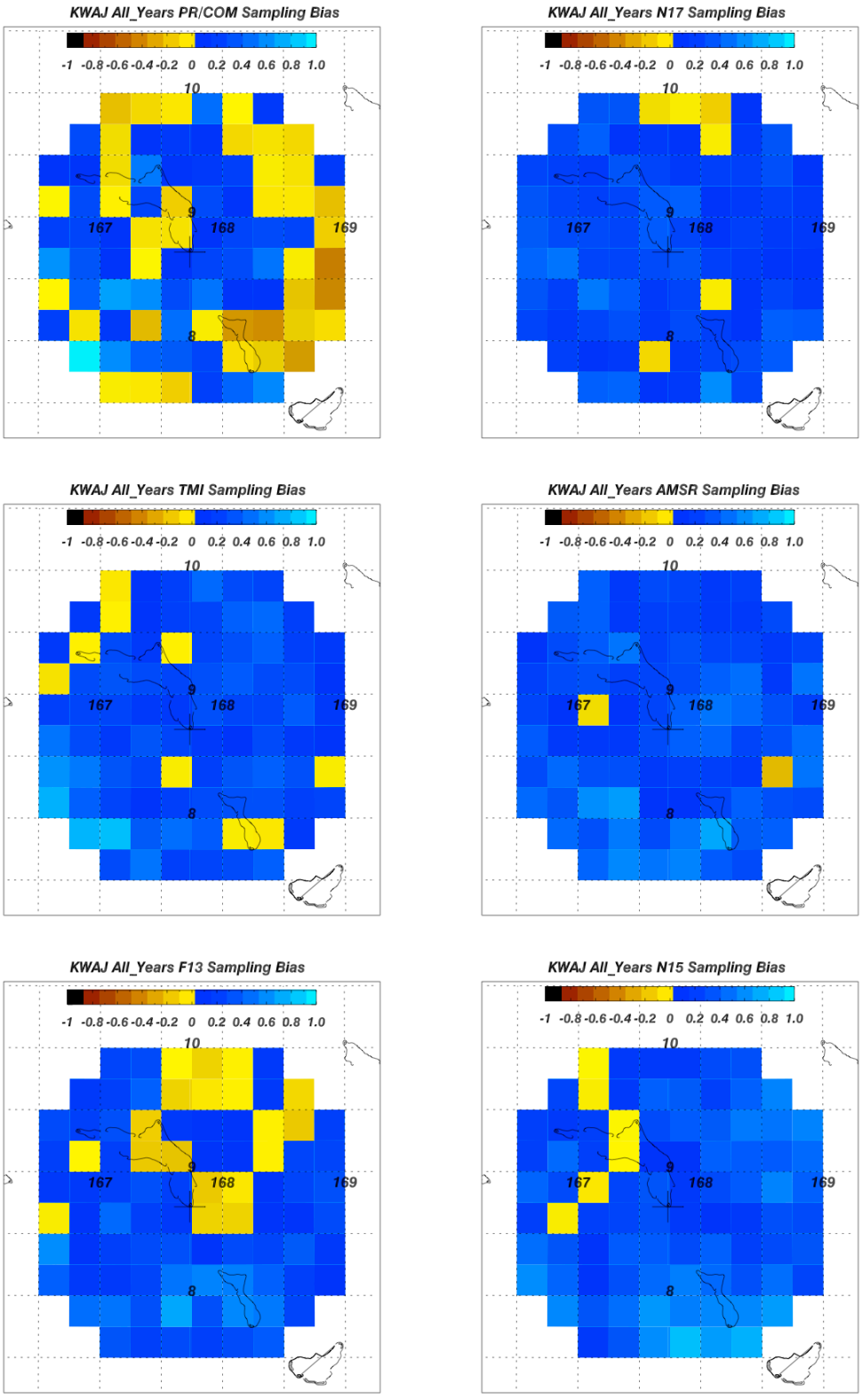

Fig 13 Geographical distribution of sampling biases for KWAJ considered for the entire study period (2003-2008).

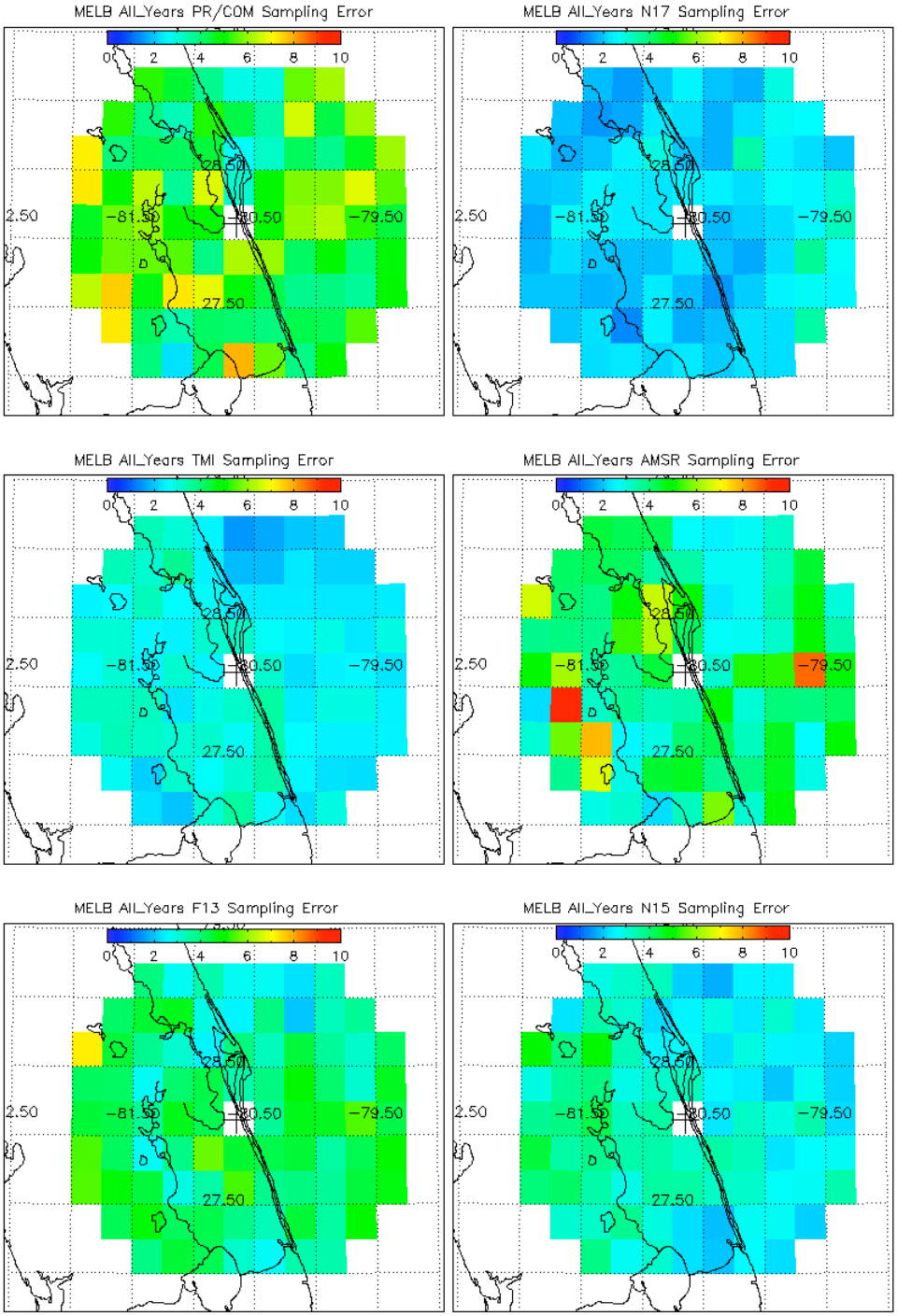

Fig 14 Geographical distribution of sampling errors for MELB in mm day^{-1} considered for the entire study period (2003-2008).

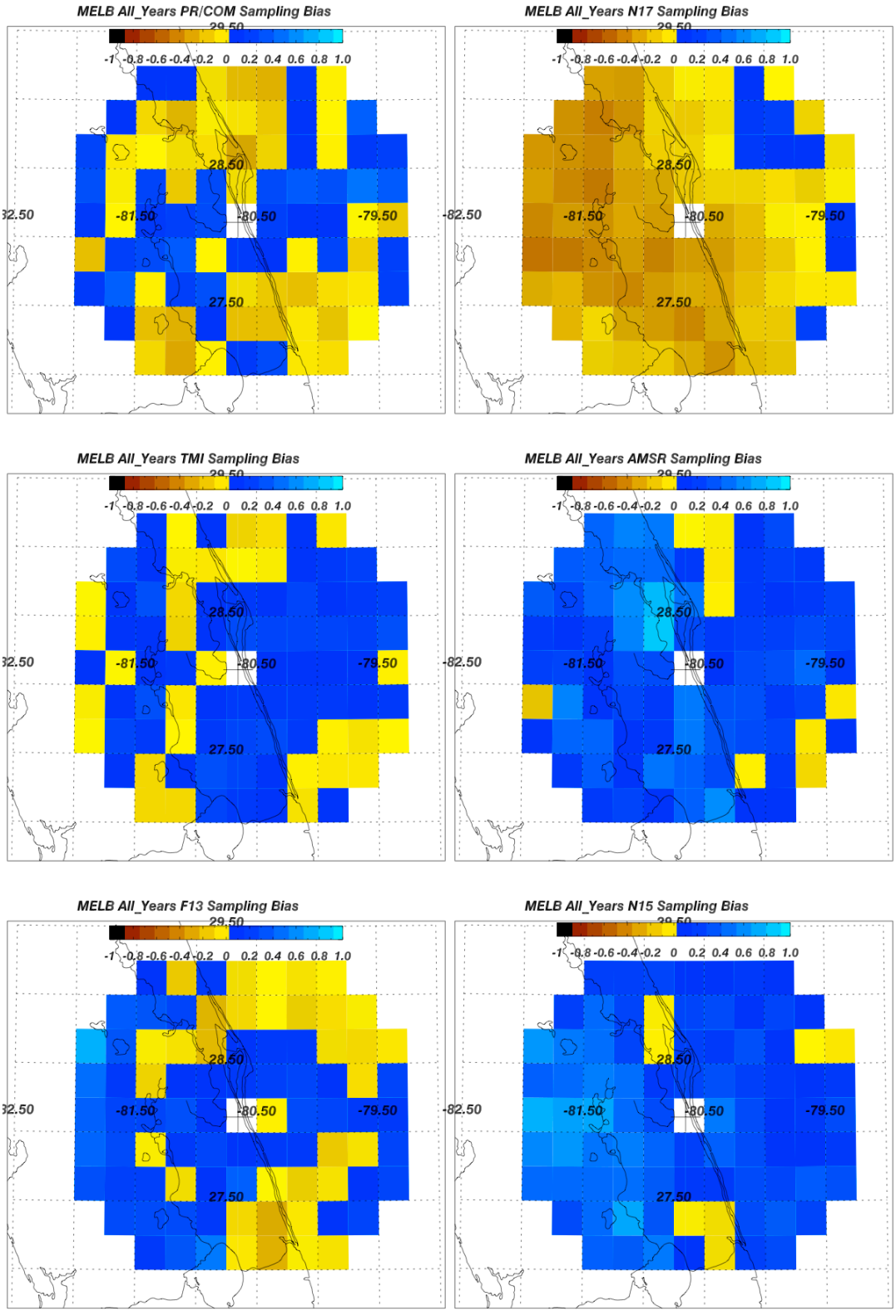

Fig 15 Geographical distribution of sampling biases for MELB considered for the entire study period (2003-2008).

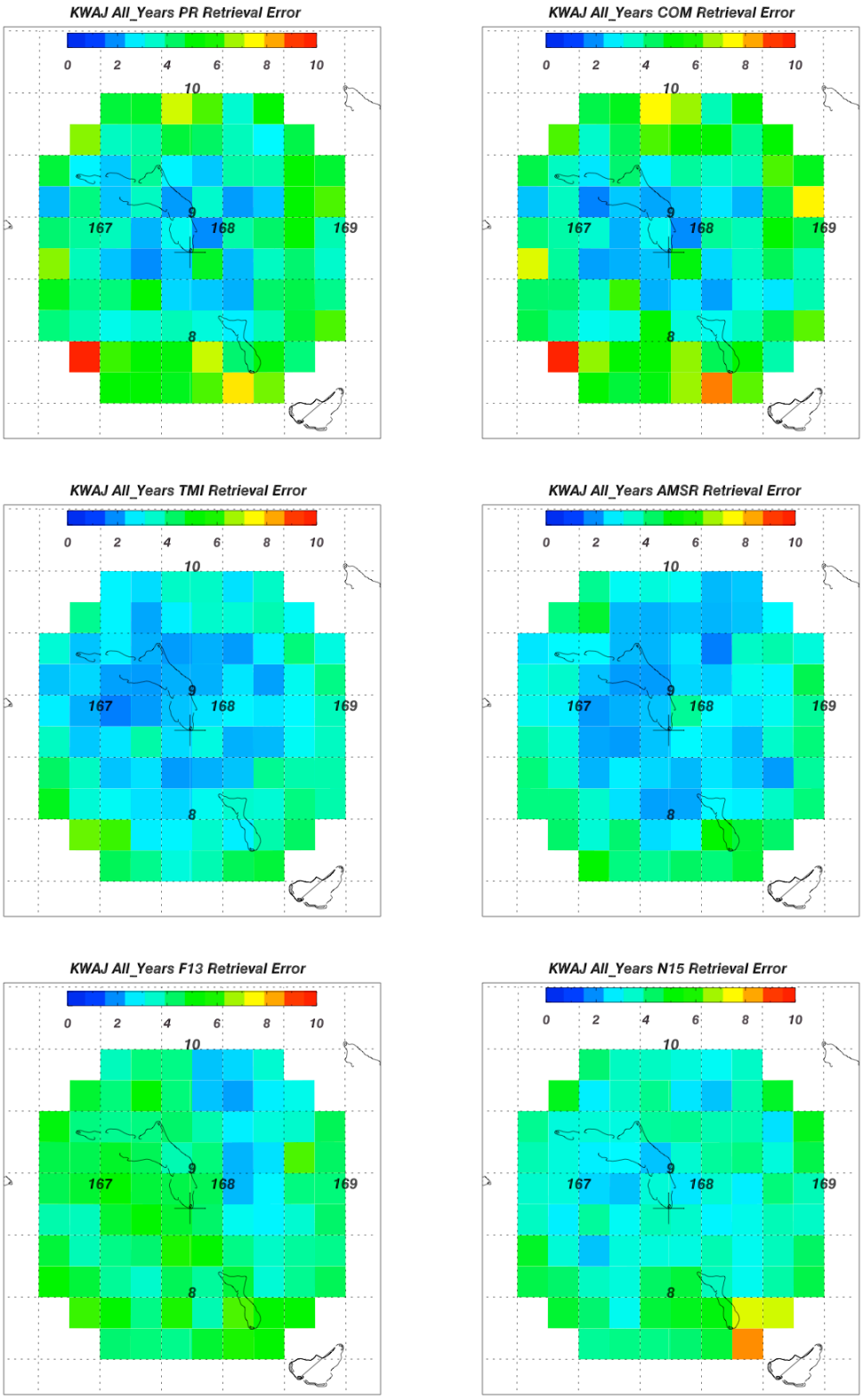

Fig 16 Geographical distribution of retrieval errors for KWAJ in mm day^{-1} considered for the entire study period (2003-2008).

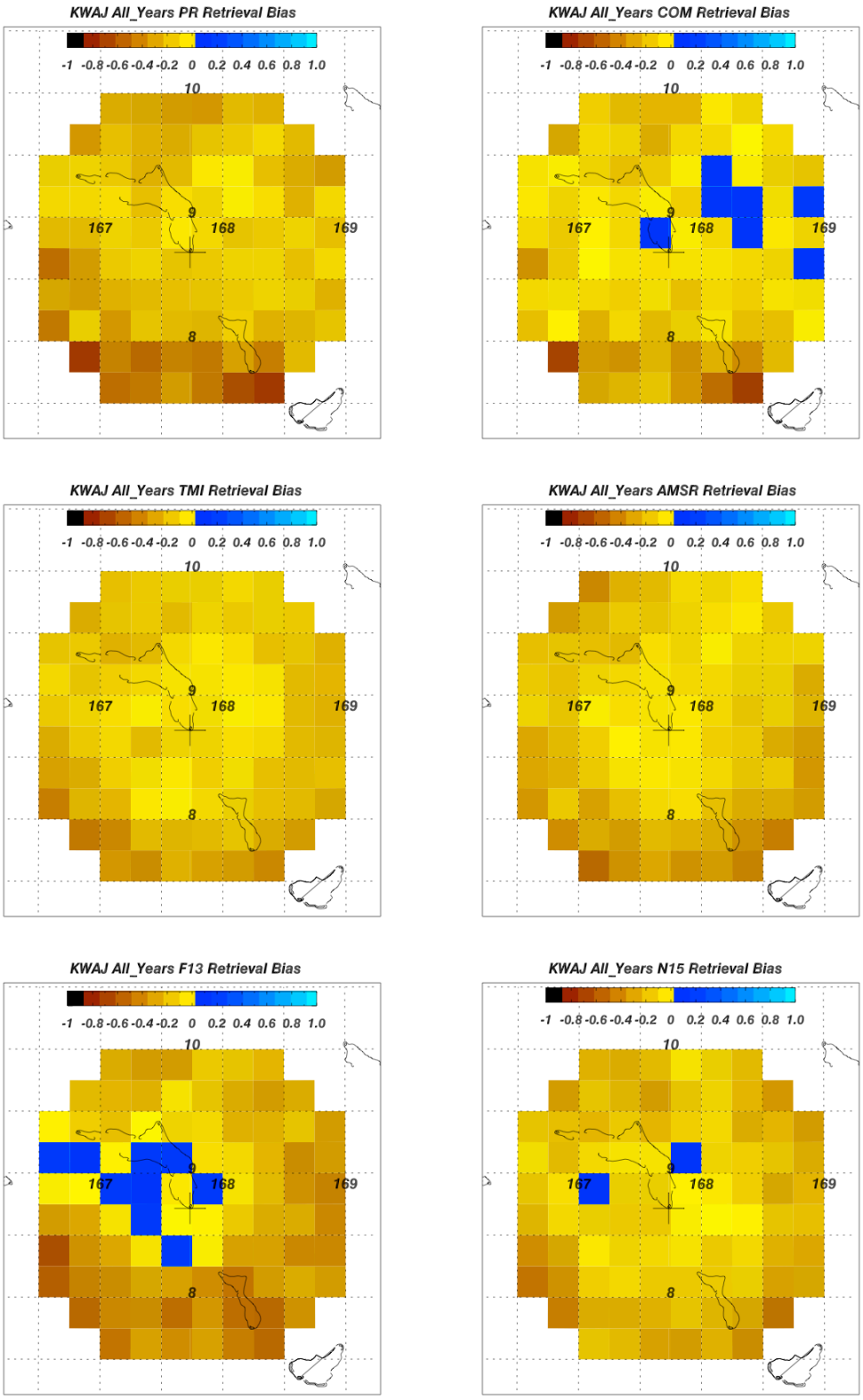

Fig 17 Geographical distribution of retrieval biases for KWAJ considered for the entire study period (2003-2008).

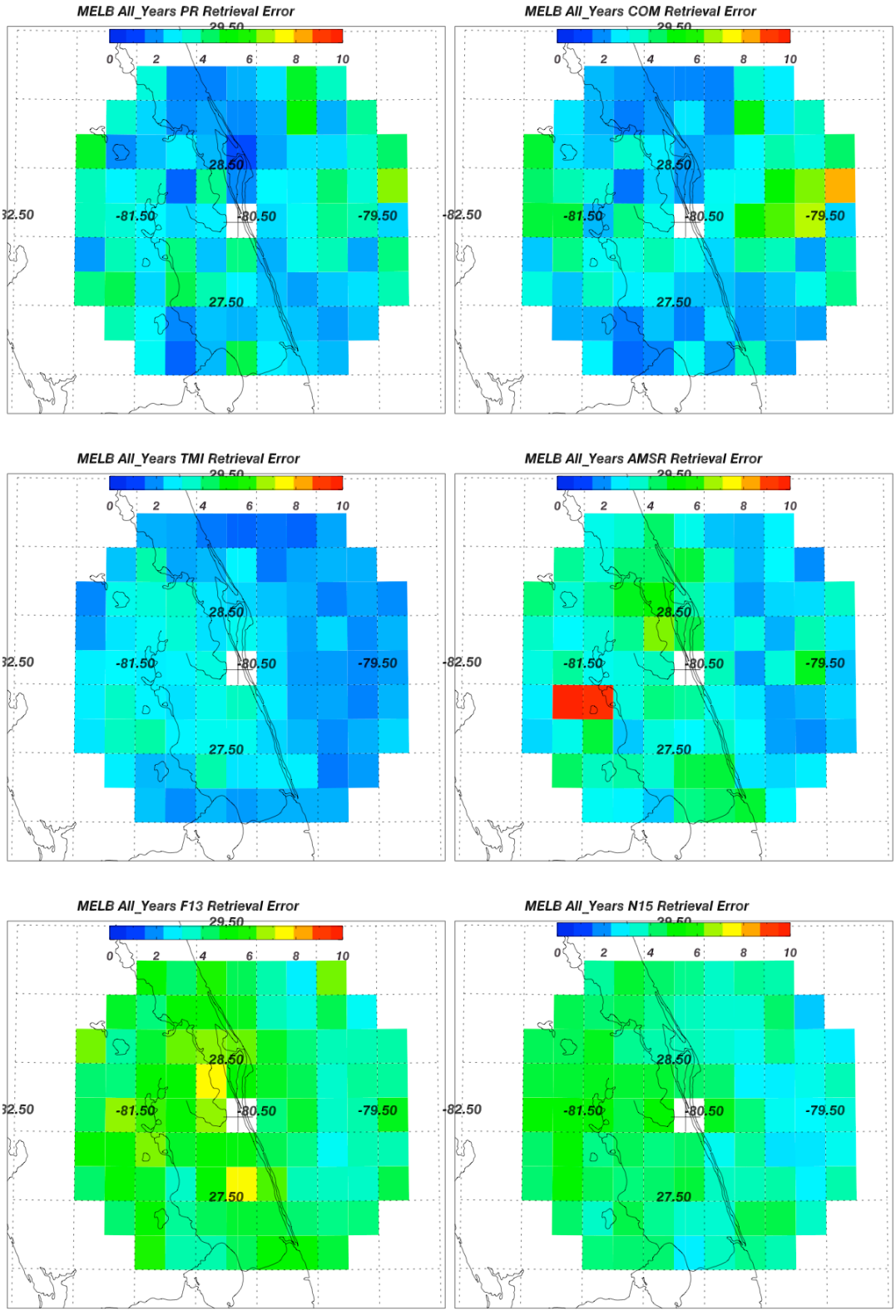

Fig 18 Geographical distribution of retrieval errors for MELB in mm day^{-1} considered for the entire study period (2003-2008).

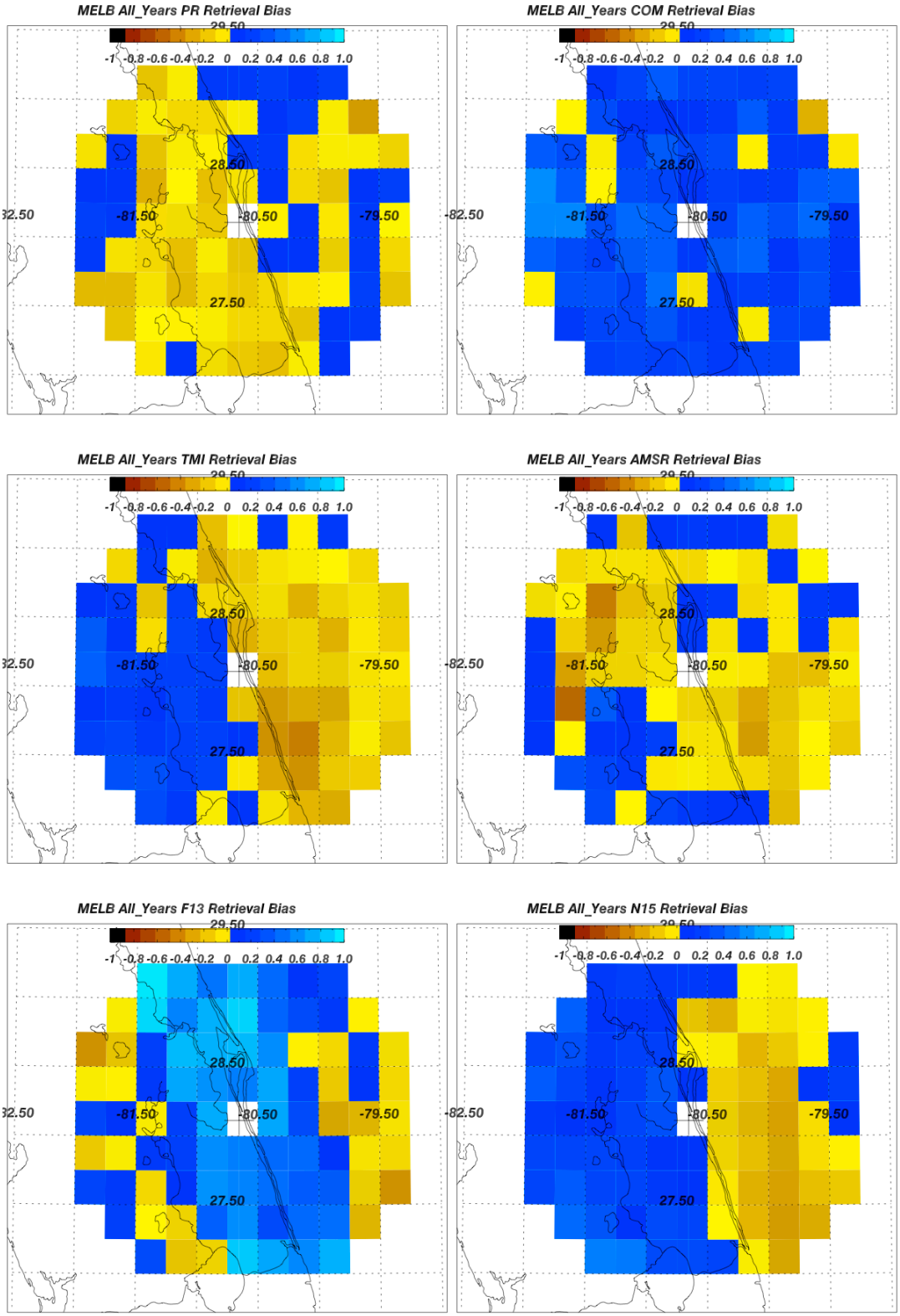

Fig 19 Geographical distribution of retrieval biases for MELB considered for the entire study period (2003-2008).